

Ecole Centrale de Nantes



Automatic Department of Ecole Central de Nantes

LABORATORY of PRISME

HEI Campus Centre, Châteauroux

THESIS presented on **27/08/2018** by:

Housseyné NADOUR

Supervised by:

Karim BELHARET

In order to obtain : Master 2 diploma in Automatic

Design, Modeling and Control of a Manipulator Robot to Positioning a Magnetic Actuator Around the Patient's Head

Jury Members :

Guy Lebret MCF, Ecole Centrale de Nantes, LS2N, CNRS

Malek Ghanes Professeur, Ecole Centrale de Nantes, LS2N, CNRS

Abdelhamid Chriette MCF, Ecole Centrale de Nantes, LS2N, CNRS

Karim Belharet Enseignant-Chercheur, HEI Campus Centre



INSTITUT NATIONAL
DES SCIENCES
APPLIQUÉES
CENTRE VAL DE LOIRE



Abstract :

Hearing loss is a common chronic condition among older adults especially the sensorineural, which is caused by damage to the hair cells of the inner ear. Surgical doctors have little ability to reliably access the complex anatomy of the inner ear and thus are unable to cure it. The CochleRob project comes to handle this obstacle by introducing therapeutic SPMNs (Super Paramagnetic Nanoparticles) in the inner ear and *control it using a magnetic actuator positioned around the patient's head by the mean of a robotic platform.*

In this context my work comes to develop a novel robotic platform and control it via a computer. We proceeded, at first, to study the effective specifications needed for the robotic platform (especially the work space, the required degrees of freedom, and the compactness).

Then, after analyzing the preliminary works done before in the project and discovering some other relevant medical mechanisms, we developed a novel robot manipulator that fulfil all the required specifications showing the rational behind the choice of the mechanism together with its motorisation as well; Beside, The mechanism was portrayed and designed by the mean of SolidWorks.

In the next step, we established the different necessary models (Geometric, Kinematic, and Dynamic models) to demonstrate the system state model and control it as well. Hence, the last chapter was dedicated for tuning a control law, explaining the rational point behind the strategy that allowed us to introduce, in a straightforward manner, controllers like PI and Loop-shaping.

As for simulation, the structure designed using Solidworks was exported to Sim-Mechanics environment, then used to validate the different models and the tuned control law.

Finally, After printing the different mechanism organs, they were jointed together to make a prototype controlled via a computer using Labview software and Maxon controllers.

Acknowledgement :

This work could never have been completed without the assistance of numerous individuals, to which I am delighted to pay tribute: My parents, my supervisor Karim Belharet, and his team: Azaddien Zarrouk, Manel Abbes, and Walid Amokrane.

Contents

Contents

Abstract	3
Acknowledgement	3
List of Figures	8
1 Introduction	9
1.1 The CochleRob project	9
1.1.1 The project motivation	9
1.1.2 The project description	10
1.2 The different treatments methods of hearing loss (administration routes)	10
1.3 The operating principle of the intracochlear drug delivery using super-paramagnetic nano-particles	11
1.4 The cochlea anatomy	12
2 Design of the robotic platform:	13
2.1 The magnetic actuator operating principle	13
2.2 State of the art:	15
2.2.1 First manipulator 6 DoF: serial robot	15
2.2.2 Second manipulator of 3 DoF: Spherical Remote Center of Motion (RCM))	16
2.3 The problematic (the desired specifications)	17
2.4 The Solution	18
2.4.1 The work space and the number of degrees of freedom	18
2.4.2 Tuning the mechanism in order to have rotational movements (ψ and ϕ)	19

CONTENTS

2.4.3	Tuning the mechanism in order to have linear movements (X,Y) , and Z	22
2.4.4	Design (CAO), motorisation, SimMechanics	26
3	Modelling	35
3.1	Direct Geometric Model	36
3.1.1	The geometric model of the delta structure with respect to R_1	37
3.1.2	Transformation from R_1 to R_0	46
3.1.3	Validation	48
3.2	Inverse Geometric Model	49
3.2.1	Transformation from the vector P_0 to the vector P_1	49
3.2.2	The inverse geometric model of the parallel structure	50
3.2.3	A novel alternative IGM of the delta structure	50
3.2.4	Validation	56
3.3	Direct kinematic model	57
3.3.1	Validation	60
3.4	Inverse Kinematic Model	61
3.4.1	Validation	64
3.5	The Dynamic Model	65
3.5.1	The dynamic model of the delta structure	66
3.5.2	The dynamic model of the serial structure	71
3.5.3	Validation	73
4	Control	76
4.1	The state model	76
4.2	The control strategy	78
4.3	The electrical subsystem control	79
4.4	The mechanical subsystem control	81
4.5	Validation (SimMechanics)	89
4.6	Experimentation	92
5	Conclusion and perspectives	95

List of Figures

Contents

1.1	The morphology of the human ear [1]	12
1.2	The cochlea [2]	12
2.1	The magnetic actuator[3]	14
2.2	Distribution of magnetic gradient line for the two configurations (for $\theta = 60^\circ$). Greater is the magnetic interaction between magnets, more the color turns on yellow [3]	14
2.3	The first robotic platform adopted, using Fanuc robot [3]	15
2.4	The second solution [2]	16
2.5	The mechanism kinematic [2]	17
2.6	Positioning the forces support in the space	18
2.7	The sphere in which the L_2 should travel	19
2.8	Preliminary and approximative space of work that covers the head .	19
2.9	(a) Prime RObot for Minimally Invasive Surgery, (b)Parallel Basic Spherical Mechanism	20
2.10	(a) Prime RObot for Minimally Invasive Surgery, (b)Parallel Basic Spherical Mechanism	20
2.11	DIAMOND Eye Surgery Robot	21
2.12	Parallel spherical mechanism	21
2.13	Collision between some organs	22
2.14	Serial spherical mechanism	22
2.15	Mechanism of 6 DoF with a linear structure in its base	23
2.16	Kinematic scheme for Otelo robot	24
2.17	Hand writing	25
2.18	Hand writing [?]	25
2.19	Design of an hybrid robot of 5 DoF, View 1	27
2.20	View 2	28

LIST OF FIGURES

2.21 View 3	28
2.22 View	29
2.23 View	30
2.24 Maxon motor-gear	33
2.25 Maxon controller	33
3.1 The geometric model input and output	36
3.2 Transformations between frames	36
3.3 Direct geometric model of the hybrid robot	37
3.4 Direct geometric model of the delta structure R_i	37
3.5 The kinematic chains	38
3.6 Translation of segments l_1 and l_2	38
3.7 the simplified structure	39
3.8 the simplified structure	39
3.9 The different coordinates systems R_i	40
3.10 The Isosceles pyramid $C_1C_2C_3P$	42
3.11 Representation of objects used in DGM	43
3.12 direction of the unit vector ω	44
3.13 The controlled point (the attractive point)	46
3.14 Direct geometric model of the serial part	46
3.15 Transformations between frames	47
3.16 Simulink diagram to validate the DGM	48
3.17 The error of the DGM	48
3.18 Inverse Geometric Model inputs and outputs	49
3.19 Inverse Geometric Model inputs ans outputs	49
3.20 Inverse Geometric Model of the parallel structure	50
3.21 The projection of P onto the plane ox_iz_i	51
3.22 The intersection of K_i with K'_i	52
3.23 The angle β_i sense	53
3.24 A_i is the projection of P , when it is a singularity point	54
3.25 Singularity points	55
3.26 Simulink diagram to validate the DGM	56
3.27 The error of the DGM	56
3.28 Simulink diagram	60
3.29 The contrast between the analytic DKM and the SimmMechanics DKM	61
3.30 The triangle $A_iB_iC_i$	63
3.31 Simulink diagram to validate the DGM	64
3.32 The error of the DGM	65
3.33 The gravity with respect to the delta structure	67
3.34 The different coordinates systems R_i associated to the slider	67

LIST OF FIGURES

3.35 Equivalent masses	68
3.36 component of Z with respect to the parallel segments	69
3.37 The forces applied on each elbow C_i	70
3.38 The projection of the force f_3 on the plane Oxz_3	70
3.39 The substantial forces that generate T_{4g}	71
3.40 The relation between the pulley rotation and ψ	72
3.41 Simulink diagram to test the dynamic model	73
3.42 Torque error signal of the delta structure	74
3.43 Torque error signal of the fourth actuator	74
3.44 Torque error signal of the fifth actuator	74
 4.1 State model diagram	77
4.2 State model diagram	78
4.3 Nyquist diagram of T	80
4.4 Bode diagram of T	81
4.5 The control scheme	82
4.6 The process with respect to the loop shaping boundaries	83
4.7 The process with respect to the loop shaping boundaries	84
4.8 Frequency plots for phase load compensator[4]	84
4.9 Frequency plots for phase load compensator	85
4.10 Figure (a): The Nyquist diagram for the open loop system $L(s)$. Figure (b): The frequency plots for the sensitivity functions $S(s)$. .	86
4.11 Frequency plots for the open loop system	87
4.12 Nyquist theorem	87
4.13 Simulink diagram for loop shaping control	88
4.14 Simulation of loop shaping controller	88
4.15 The Simlulink diagram for the whole closed loop system	89
4.16 Comparison between the references and the measurements of the angels	90
4.17 The current measurements (1 unit = 1 A)	91
4.18 The prototype	92
4.19 The prototype	93
4.20 The prototype	93
4.21 The motors angels and the references (screen capture for LabVIEW) .	94
 5.1 A cube inside the work space of the delta robot [5]	96
5.2 Delta robot of 4 degrees of freedom	97

Chapter 1

Introduction

Contents

1.1	The CochleRob project	9
1.1.1	The project motivation	9
1.1.2	The project description	10
1.2	The different treatments methods of hearing loss (administration routes)	10
1.3	The operating principle of the intracochlear drug delivery using superparamagnetic nano-particles	11
1.4	The cochlea anatomy	12

1.1. THE COCHLEROB PROJECT

1.1.1. THE PROJECT MOTIVATION

Deafness is the third most spread chronic condition in older adults, affecting 52% of adults over the age of fifty. According to scientific studies, there is a strong relationship between the severity of hearing loss and conditions of life, as hearing impairment constrains educational achievement and employment options. Moreover, congenital deafness is a common birth phenomenon, affecting about 1 in 500 births and interrupting the normal acquisition of languages. The damage to the cochlea of the inner ear brings the most common form of hearing loss (sensorineural).

Several surgical options are available for many other kinds of hearing loss, Nevertheless, otologists are currently unable to reliably access the inner ear without causing irreversible injury, which makes the human dexterity useless to treat this kind of deafness [6].

1.1.2. THE PROJECT DESCRIPTION

In this context, the aim of the CochleRob project (funded by the laboratory of PRISME, in collaboration with Dijon University Hospital and SIEMEL INDUSTRIE) is the development of an intra cochlear drug delivery technique in order to treat the sensorineural hearing loss. In the proposed system, the therapeutic agent will be transported by super paramagnetic nanoparticles (SPMN), which can be moved in the inner ear under the effect of forces generated by a magnetic actuator. In that way, there is no necessity to any manual access that can damage the inner cochlea.

1.2. THE DIFFERENT TREATMENTS METHODS OF HEARING LOSS (ADMINISTRATION ROUTES)

For several years the inner ear drug delivery has become a challenge in the treatment of sensorineural hearing loss [7]. Recent advances in molecular therapy and nanotechnology have stimulated the development of a variety methodologies such as systemic and intratympanic or even directly intracochlear way through an injection into the inner ear [7]. The treatment of the inner ear is limited by the low concentration achieved with systemic delivery because a blood-cochlear barrier exists, which is anatomically and functionally similar to the blood-brain barrier [8]. High systemic doses must be administered in order to obtain inner ear therapeutic concentrations [9]. The necessity of long-term treatment and significant adverse effects limit furthermore the use of systemic administration [10]. It is therefore necessary to develop safe and reliable mechanisms for the direct delivery of drugs into the inner ear. Methods for local delivery can be categorized as either intratympanic or intracochlear approaches. The minimal invasive method of local drug administration to the inner ear used for several years in clinical practice is to inject the drug into the middle ear cleft through the tympanic membrane under local anesthesia. In this way, the drug is in contact with the RWM for an undetermined time, and subsequently diffuses through the membrane into scala tympani. However, the delivered quantity of therapeutic agent to the inner ear is poorly controlled by this method since the drug is easily evacuated through the Eustachian tube to the pharynx [11]. This method is also limited by the RWM and the absence of the perilymphatic flow allowing the drug diffusion towards the apex of the cochlea. Indeed, contrary to the systemic circulation the perilymphatic and endolymphatic flow is extremely low. Passive diffusion towards the apex of the cochlea is thus complicated due to its length, resulting in a large gradient from the base to the cochlea [12]. Side effects are lower compared to systemic delivery but remains high doses to achieve intracochlear therapeutic concentration. In ad-

dition, the amount of drug through the RWM is very variable depending on the individual anatomy [11] [13]. Intracochlear injection enable precise and efficient administration of the drug. This pathway is against much less accessible and risky due to the creation of a perilymph fistula and the hydrostatic pressure generated by the injection. Because of this fistula, perilymph leakage is inevitable and the loss of injected drug must be taken into account [14].

1.3. THE OPERATING PRINCIPLE OF THE INTRACOCHLEAR DRUG DELIVERY USING SUPER-PARAMAGNETIC NANO-PARTICLES

Magnetic nanoparticles represent a promising solution as a drug carrier in the inner ear as they move into the cochlea with minimal hydrostatic force under the effect of externally applied magnetic field [15]. Magnetic nanoparticle driving was first reported using magnets [16] or superconducting magnets [17]. Martel et al proposed to use the gradient generated by clinical MRI to pull the particles [18]. MRI driving and trajectory of magnetic nanoparticles can be modeled and preplanned [19]. These untethered particles can navigate in body fluids to allow a number of new minimally invasive therapeutic and diagnostic medical procedures. Indeed, the development of untethered microdevices that can be steered in the blood vessels could benefit several minimal invasive surgeries or interventions [20]. However, as the overall size of the micro devices is reduced, it becomes technologically more challenging to propel them. Among the different propulsion mechanisms that have been proposed ([21], [22], [23], [24]). Therapeutic magnetic micro carriers (TMMC) guided in real time by magnetic field gradients system are actually experienced as mean to improve drug delivery to tumor sites. One solution that has been validated *in vivo* is the use of the magnetic field and magnetic gradients generated by a clinical magnetic resonance imaging (MRI) system as the energy source for propulsion [24]. Magnetic iron-cobalt nanoparticles encapsulated into biodegradable poly (D,L-lactic-coglycolic acid) (PLGA) microparticles with the appropriate saturation magnetization (M_s) have been successfully used in animals. Similar wireless control navigation of intraocular micro particles has been applied in ophthalmic procedures for drug delivery purposes [25]. Complex non-uniform magnetic fields and high magnetic gradients, generated by an OctoMag electromagnetic system, allowed less invasive and safer retinal surgery, and provide as well an increased level of dexterity desired by clinicians.

1.4. THE COCHLEA ANATOMY

The ear contains three parts : external ear (auricle), middle ear (tympanic) and inner ear (labyrinthine). The inner ear contains both the organ of hearing: the cochlea and the organ of balance:

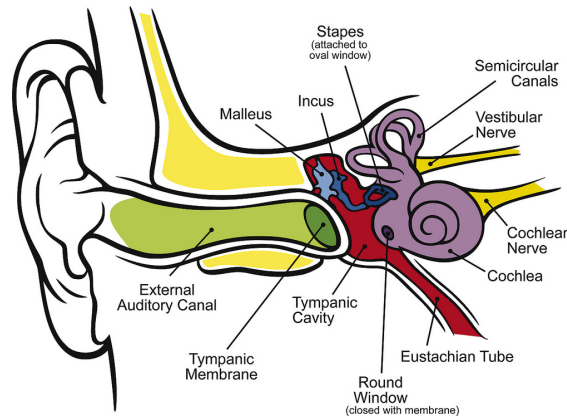


Figure 1.1: The morphology of the human ear [1]

The cochlea is responsible of transforming acoustic signals into neural pulses which are then emitted to the brain. It can be viewed as a set of membranous tubes, 31-33mm in human. This tube is coiled much like a snail shell to form two and a half turns around its axis. The height of the bony cochlea is 4mm and the width of its basal coil, which is the largest, is 7mm (see the figure below)[2]

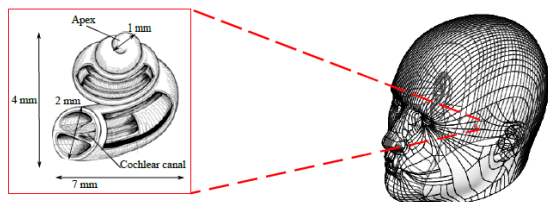


Figure 1.2: The cochlea [2]

Chapter 2

Design of the robotic platform:

Contents

2.1	The magnetic actuator operating principle	13
2.2	State of the art:	15
2.2.1	First manipulator 6 DoF: serial robot	15
2.2.2	Second manipulator of 3 DoF: Spherical Remote Center of Motion (RCM))	16
2.3	The problematic (the desired specifications)	17
2.4	The Solution	18
2.4.1	The work space and the number of degrees of freedom	18
2.4.2	Tuning the mechanism in order to have rotational movements (ψ and ϕ)	19
2.4.3	Tuning the mechanism in order to have linear movements (X, Y), and Z	22
2.4.4	Design (CAO), motorisation, SimMechanics	26

2.1. THE MAGNETIC ACTUATOR OPERATING PRINCIPLE

There are multiple solutions for propelling the microrobot in a viscous medium, the solution adopted and developed by the laboratory team is to use permanent magnets. Such magnetic actuation systems are able to generate magnetic fields that can apply effective forces and torques to a magnetic device in a compact form-factor.

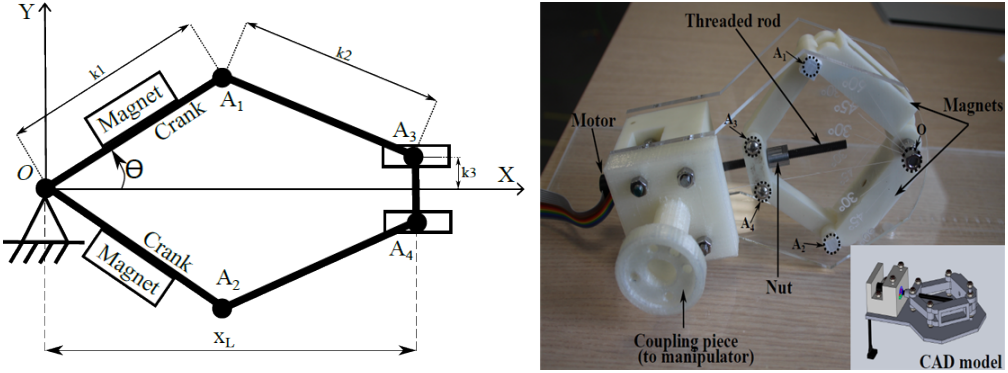


Figure 2.1: The magnetic actuator[3]

Multiple permanent magnets are put closed to each other, but separated with an angle θ . Positioning two magnets, as illustrated above, generates two essential magnetic points in space (two Lagrangian points L_1 and L_2)[3]:

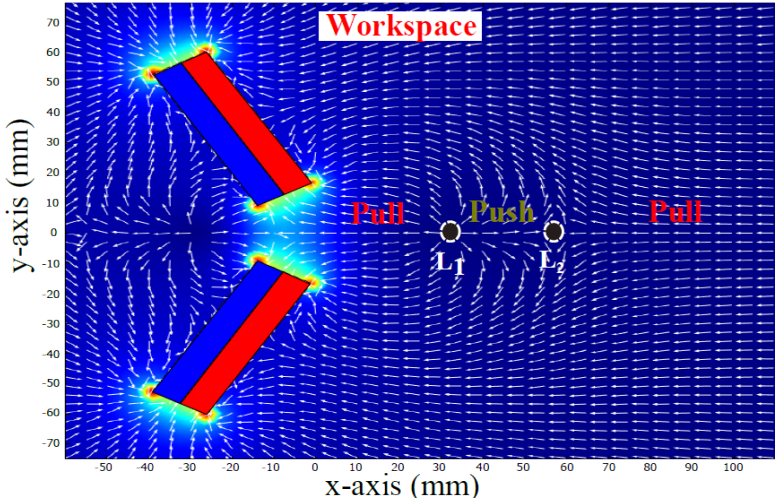


Figure 2.2: Distribution of magnetic gradient line for the two configurations (for $\theta = 60^\circ$). Greater is the magnetic interaction between magnets, more the color turns on yellow [3]

The actuator represented above combines two permanent magnets that makes possible to create both push and pull forces as it is illustrated. That makes L_1 a repulsive point, whereas L_2 an attractive one. By the mean of L_2 , the particles can moved in the viscous liquid of the inner ear.

The Lagrangian points position, are decreasing functions of the angle separating the two magnets, Whereas the length forces are increasing functions. Nevertheless, for technical issues, θ must be between 30° and 60° .

2.2. STATE OF THE ART:

The robotic team of PRISME laboratory aims to develop a robotic platform, that can demonstrate the administration of drug in the patient head (eye, ear, brain...) using super-paramagnetic nanoparticles. This platform is composed of three subsystems : a magnetic actuator based on permanent magnet, a tracking vision system and a manipulator arm.

In this context, our work comes to contribute and design a suitable manipulating robot that can fulfil all the desired specifications. At first, we described briefly the different manipulators that have been already used and proposed in project. mentioning obviously other inspiring manipulators that can have a potential solution.

2.2.1. FIRST MANIPULATOR 6 DOF: SERIAL ROBOT

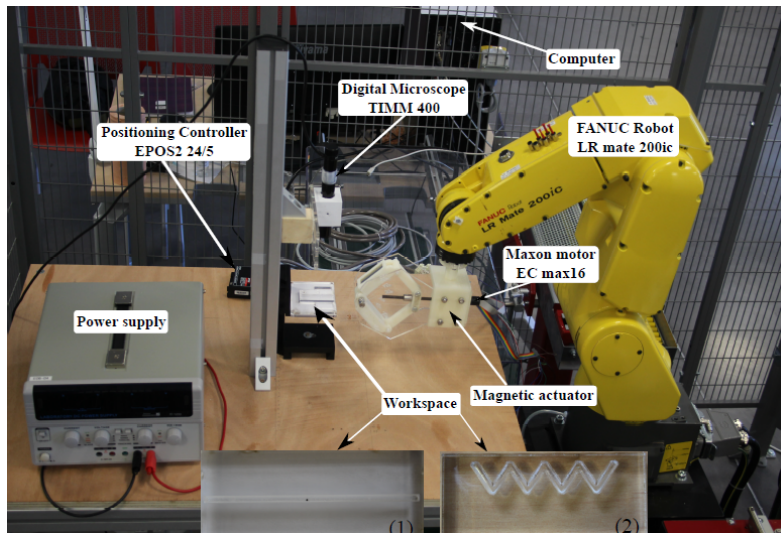


Figure 2.3: The first robotic platform adopted, using Fanuc robot [3]

The serial robot used is FANUC LR Mate 200iD (6 DOF). However, this platform is used just to show the operating principle of the actuator, and it cannot be the commercialized platform for multiple reasons:

- The task needed does not require a manipulator robot of 6 DoF. Otherwise, there will be redundancy.
- The used robot space work is not compatible with the sphericity of the head (The space work centre of the robot is far away from the head), that effects the next point:

- The space work needed here in order to position the magnetic actuator, is not completely reachable by the robot end-effector. Although it is possible to introduce another serial manipulator whose the space work includes completely the space work needed to be reached. But as result, the robot will be quiet bulky as well.

2.2.2. SECOND MANIPULATOR OF 3 DOF: SPHERICAL REMOTE CENTER OF MOTION (RCM))

According to [2], this solution has been introduced because the desired kinematic structure has to be able to guide the actuator in 3D-space by realizing a spherical movement whose center is situated away from the structure, [and nearby] the center of the cochlea. The most suitable mechanisms in this case are the mechanical Remote Center of Motion (RCM) ones which are classified in [26].

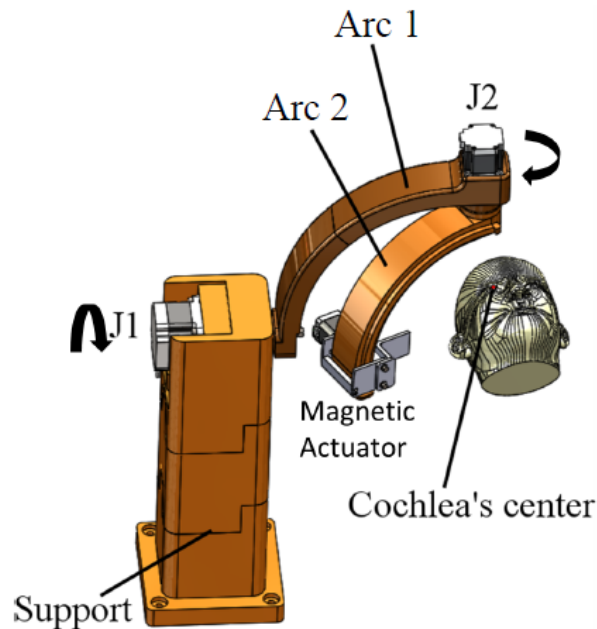


Figure 2.4: The second solution [2]

The structure represented above has 3 degrees of freedom. This mechanism is equivalent to a serial spherical system. It can be represented by three revolute joints with concurrent axes J1,J2 and J3 (see the following figure).

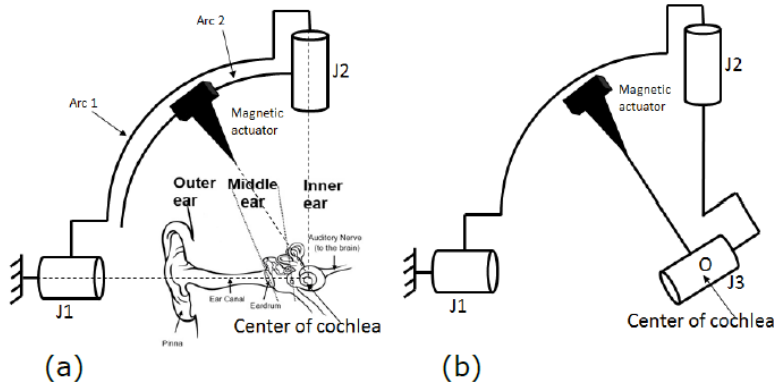


Figure 2.5: The mechanism kinematic [2]

This solution has the benefit of that the robot work space includes completely the desired work space. However it still does not fulfil all the desired specifications explained in the next section :

- The structure can orientate the forces around the cochlea center, but without being able to move the orientations center because it has no linear movement. Hence a manual adjustment of the robot with respect to the cochlea is still required in this case.
- The structure has three rotational joints, whereas there must be just two rotational movements in order to orientate a vector/force in 3D space. This is redundancy unless if the objective of third joint is to have a flexible manipulator and avoid any collision between it and the patient body. But it is still not necessary since it is possible to handle that without adding an extra joint.

2.3. THE PROBLEMATIC (THE DESIRED SPECIFICATIONS)

Choosing a structure or another one is compelled by the following essential points and specifications:

- The actuator operating principal and its relationship with the number of degrees of freedom.
- Despite the inaccessibility to that enclosed space (The head), the shape of the work space desired to be reached must be completely included in the robot work space, taking in account the safety of patient as well.

- No manual adjustment should have place, so the motion must be completely automated (as we have seen in the second solution, there must be manual adjustment).
- The robot must be optimal as better as possible.
- The performance in term of precision and capacity so that the end-effector must be able to bear 1 kg of weight (The weight of four magnets is 800 g).

2.4. THE SOLUTION

2.4.1. THE WORK SPACE AND THE NUMBER OF DEGREES OF FREEDOM

The necessary and sufficient clue to take a decision about the number of degrees of freedom is the magnetic actuator operation principle. Returning back to the figure 2.2, we notice that the magnetic field is parallel behind the attractive point L_2 , meanwhile it is not the case between the two Lagrangien points, so the useful forces that push particles from L_1 to L_2 are born upon the axis linking these two points. Hence the objective is to position the axis (L_1L_2) in the space. To position an axis in the space, it is conceivably sufficient to position a point belonging to this axis, which is the attractive point L_2 in this case, and to orientate that axis itself around that point (L_2).

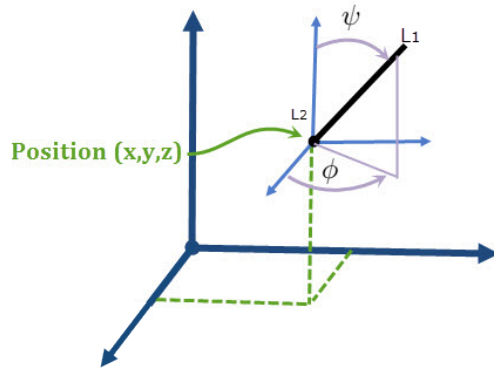


Figure 2.6: Positioning the forces support in the space

It is clear now that the necessary and sufficient number of degrees of freedom is 5. three linear movements (X, Y , and Z), and two rotational movements (ψ and phi).

The point L_2 is supposed to be able to reach the top of the head including the two cochlea on the right and the left, and other important organs like the brain and the eyes. Then let it be approximately a sphere whose the diameter is the distance between the two head temples:

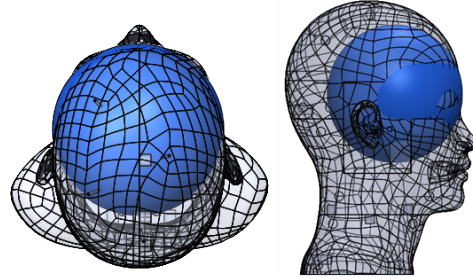


Figure 2.7: The sphere in which the L_2 should travel

Note: the point L_2 is referred to as P_1 in the modeling chapter and thereafter.

2.4.2. TUNING THE MECHANISM IN ORDER TO HAVE ROTATIONAL MOVEMENTS (ψ AND ϕ)

It is easy to imagine an unaccountable number of structure having five DoF, But proposing the convenient and suitable one depends entirely on the specifications discussed previously.

At first let us start thinking about the rotational movements ϕ and ψ , Regarding to the work space to be reached, it is vital to think about a structure that makes the actuator turns on a sphere covering the hole required work-space (the head):

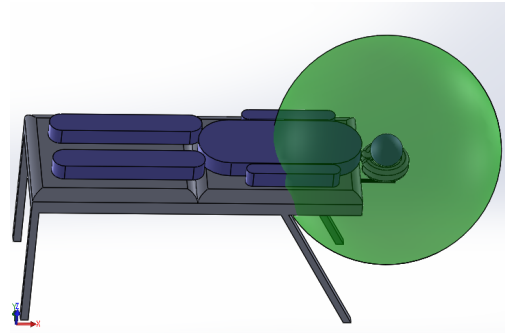


Figure 2.8: Preliminary and approximative space of work that covers the head

The best way to do that taking in account the work space specifications (the robot work space must be concentrated on the center of the work space needed to

be reached *in order to have a compact manipulator*) is to think about arcs, because it is the straightforward way to get rotational movements, this kind of mechanism is called spherical Remote Center of Motion (RCM) (see for example [26], [2]).

The relevant types mentioned in [26] are Prism RObot for Minimally Invasive Surgery and Basic Spherical Mechanism:

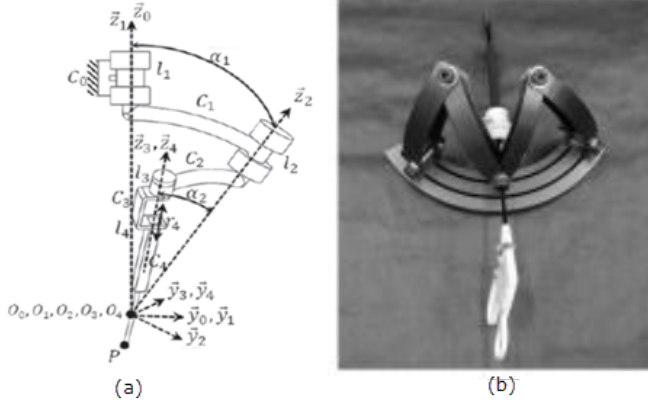


Figure 2.9: (a) Prime RObot for Minimally Invasive Surgery, (b)Parallel Basic Spherical Mechanism

Employing the Prime RObot in our platform compels having structure like presented in the following figure :

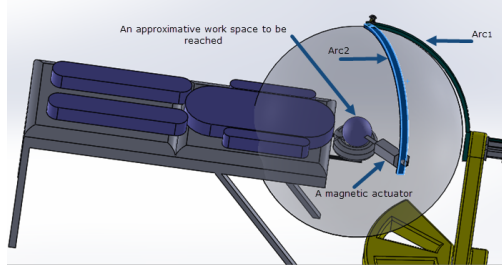


Figure 2.10: (a) Prime RObot for Minimally Invasive Surgery, (b)Parallel Basic Spherical Mechanism

This spherical and serial structure seems very simple and convenient to the process since it has a large range of orientation. However, it is not adapted for our choice of the structure that we will add to generate a linear movements. The second structure, which is also used in [27] (see the figure 2.11) is robust and rigid, but has a range of orientation smaller than the needed, Even though it is possible to increase it by making the orientations axes coincidence, it will have the problem

that it collides with the patient body.



Figure 2.11: DIAMOND Eye Surgery Robot

In addition to these spherical RCMs (that we have already thought about them before our bibliographical research), we mention other spherical mechanism that we proposed during the design of the structure. Instead of using two rotational joints, we introduce one rotational joint to generate the angle ϕ , and a sliding motion to generates the second rotation ψ . That way, there will be no worry about the patient safety. To do that, two mechanism are proposed :

The first one (the figure below) is parallel, it has the advantage that the two joints motors are fixed on an immobile point. As result, instead of having the first motor being loaded by the weight of the second one, the slider weight is shared between them, and as result, the precision is increased:

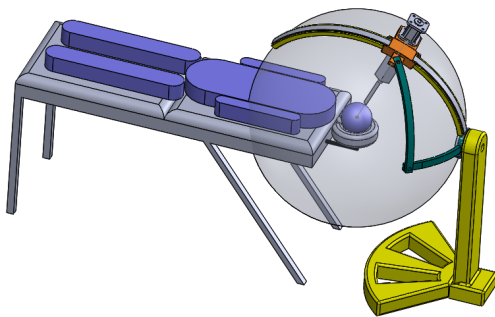


Figure 2.12: Parallel spherical mechanism

Nevertheless, this structure has as an inconvenient that it cannot cover all the desired rotation range, because of mechanical constraints (intersection between some different organs) as it is illustrated:

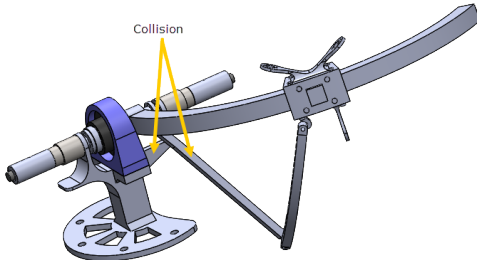


Figure 2.13: Collision between some organs

The second mechanism, which is a very simple and easy way to resolve such a problem, is by introducing a pulley and a flexible belt on which the pulley will roll; the pulley is linked to a motor rotor; the motor itself is fixed to the slider, and the belt is attached to the arc.

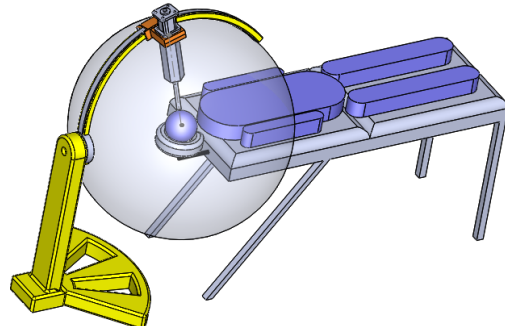


Figure 2.14: Serial spherical mechanism

2.4.3. TUNING THE MECHANISM IN ORDER TO HAVE LINEAR MOVEMENTS (X, Y), AND Z

The previous section we have discussed the necessity for a compact and safe rotational mechanism adapted with the sphericity of the enclosed space wanted to be reached (the head). Adding another mechanism is mandatory to generate linear movements, this mechanism must either carry the spherical mechanism, or be carried upon it. Thus we are facing a serial structure of two different mechanisms. We have several choices concerning the second mechanism, and it seems that the

serial structure is the simplest one. such a choice has been adopted in several previous work.

Some previous and relevant works

In a pithily thesis [28], Mathieu MIROIR went extra mile analysing and suggesting different mechanisms for otological microsurgery, the most relevant one is represented in figure 2.15.

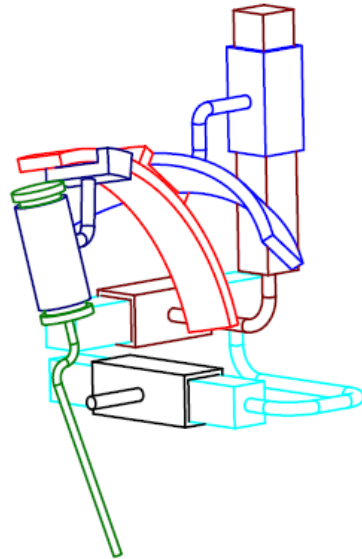


Figure 2.15: Mechanism of 6 DoF with a linear structure in its base

A similar mechanism of 5 DoF (represented below) is proposed in [28].

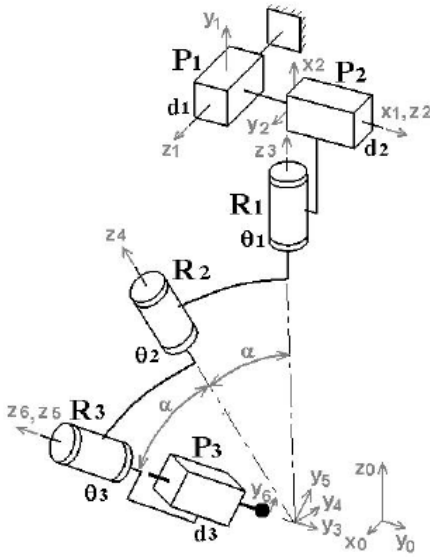


Figure 2.16: Kinematic scheme for Otelo robot

The choice of the structure

For purpose of compactness, rigidity, and precision, we tried to look for a structure that can fulfil all the specifications as better as possible. Our choice will be very different, and it will be based on the specifications wanted to be reached. For instance, the space, in which the attractive point L_2 must move, is relatively small, whereas the precision must be really high since the head organs dimensions are around just few millimetres (like the cochlea). Furthermore, the structure must be rigid and able to bear significant weights since the magnetic actuator is around 1 kg. All that must be taken in account together with the compactness.

Moving an object in a *small area (like the cochlea)* with high precision reminds us of the hand writing. When somebody wants to write a big letter he moves his whole arm since there is no need for precision, whereas when he writes a small one, then he puts his wrist on the paper and moves only his three fingers that grasp the pen together (figure below). Usually he does that intuitively in order to hold the pen roughly and firmly, as well as to increase the precision furthermore.

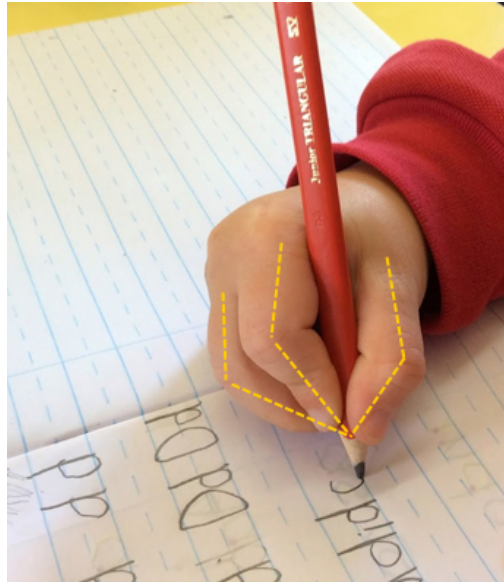


Figure 2.17: Hand writing

The shape formed by the three fingers is a parallel structure. Among all the parallel robots, the one that has the same shape and principle is the one invented by Reymond Clevé in 1985[29]. This kind of parallel robots is called Delta Robot. According to his thesis [30], the robot was developed in order to move light objects at high dynamics and he succeeded to develop the first Delta robot with four degrees of freedom [29].

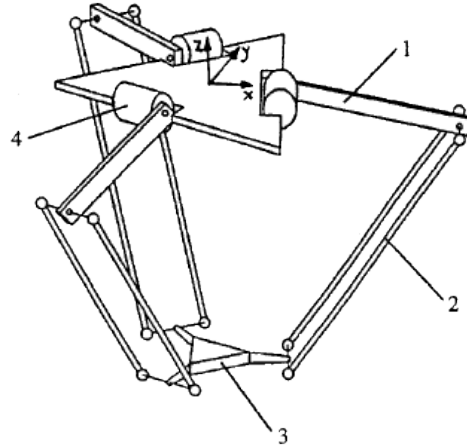


Figure 2.18: Delta Robot [31]

This structure fits well our specification. In fact, Alain Codourey, one of the

most famous developers of this kind of robot, stated that the delta robot possess a number of advantages when compared to serial arms, and the most important one is certainly the possibility to keep the motors fixed on the base which allows a large reduction of the active mobile mass of the robot structure [31]. Beside this feature, the delta robot consists of three chains, each of them is composed of two segments rather than three segments in the serial case, these two features makes *the structure more compact*. He stated also in the same article that another advantage of parallel robots is their higher rigidity, and these features allow *more precise and much faster manipulations*.

Having three chains connected to one point is meant for the purpose to pick up and place light objects (20 g) at high dynamic. However, in our case it will be meant to *increase the rigidity against the gravity* since the end-effector weight is around 1 kg, and its speed is very low as the medical operation will proceed within 6 minutes, at least.

In the same reference, it is stated that the delta robot suffers from a limited workspace. Yet, this is not an inconvenient for our case since the works space needed to be reached is relatively small.

2.4.4. DESIGN (CAO), MOTORISATION, SIMMECHANICS

The next step is to design the mechanism using SolidWorks, and to choose the suitable hardware items like motors, controllers, and many mechanical pieces as well. The following figures shows, in different perspectives, the assembly of the different organs of the robot including the chosen motors.

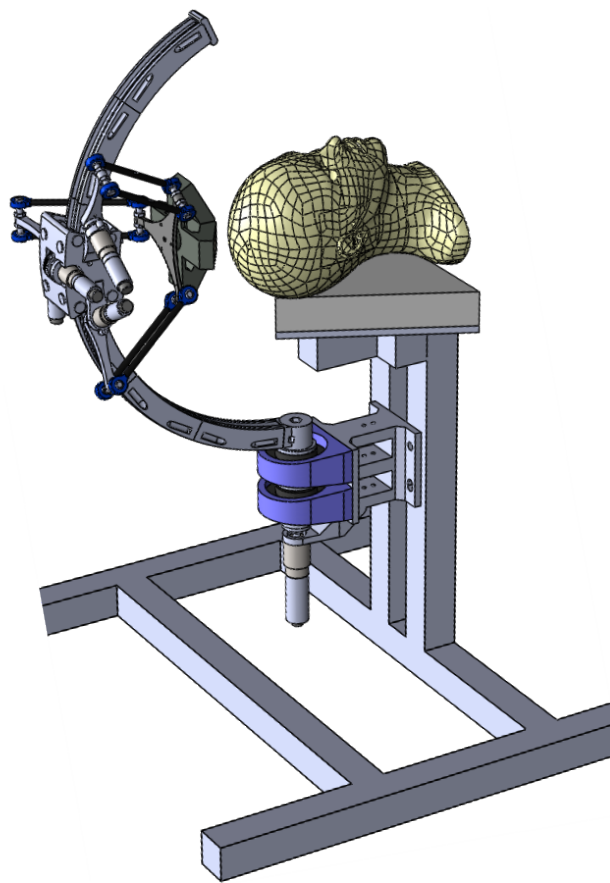


Figure 2.19: Design of an hybrid robot of 5 DoF, View 1

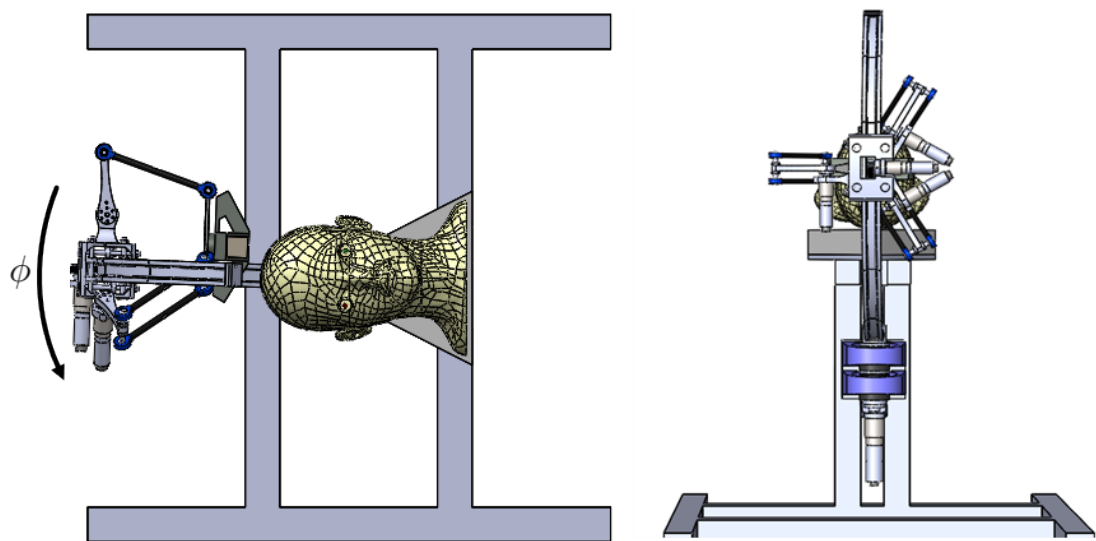


Figure 2.20: View 2

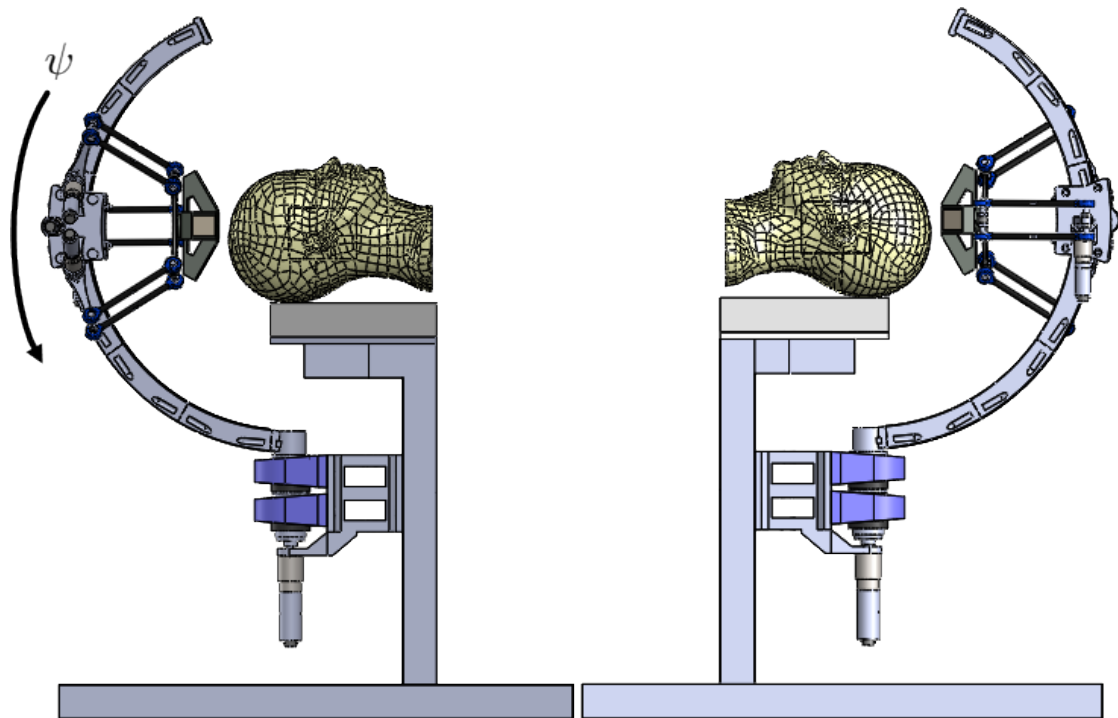


Figure 2.21: View 3

Description

This robot of 5 DoF (X, Y, Z, ψ , and ϕ), is an hybrid structure composed of a spherical serial mechanism and a parallel mechanism. It consists mainly of four parts, the support (1), the arc (the curved arm (2)), the slider (3), and the parallel structure (figure 2.23). The arc is linked to the support by a bear ball (4) and actuated by the motor (5) to generate the rotation ϕ . The slider can move smoothly on the arc thanks to 8 bear balls (6), and a pulley actuated by the motor (7). Rolling the pulley (8) on a belt (9) (pasted on the arc (10)) generates the rotation ψ . The slider itself represents a mobile base for the delta structure, which consists mainly of three identical kinematic chains (11) linking the slider with the a mobile board (12) (it is called conventionally *nacelle* in [30]). Each chain kinematic has an arm (13) and a forearm (14), joined together and with the nacelle via ball joints (15). Each forearm is linked to its corresponding motor-gear axis via a hub (16). The fact that arms are composed of two parallel segments, restricts the movement of the nacelle to pure translations with no rotation with respect to the slider. which makes it easy to control the magnetic actuator (17) linked to the nacelle. Finally, The gears (18) allows to increase 231 times the torque provided from each motor (19).

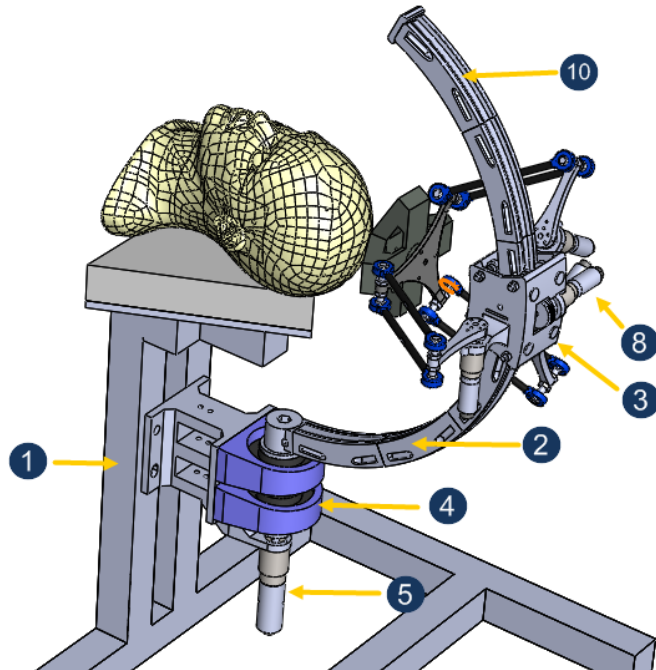


Figure 2.22: View

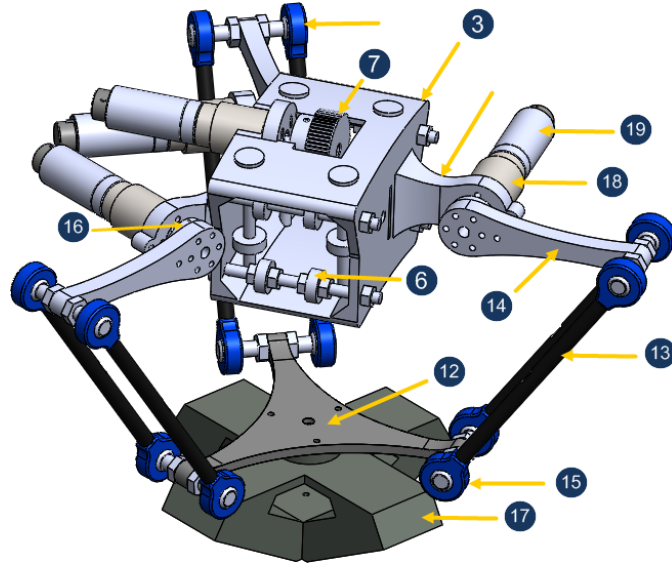
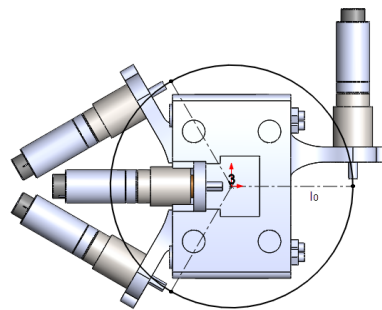


Figure 2.23: View

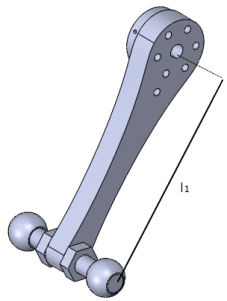
Notes about tuning of the dimensions, and the choice of the motors

The different organs dimensions are related to each other, changing one dimension affect other dimensions choices and the choice of the suitable motor (in term of space and capacity) as well. The important dimensions to be tuned are:

- The slider radius l_0



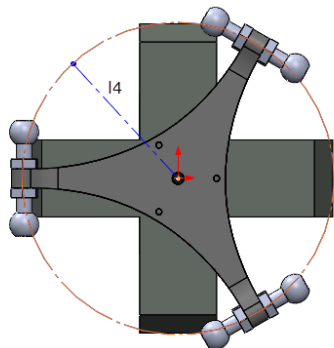
- The forearm length l_1



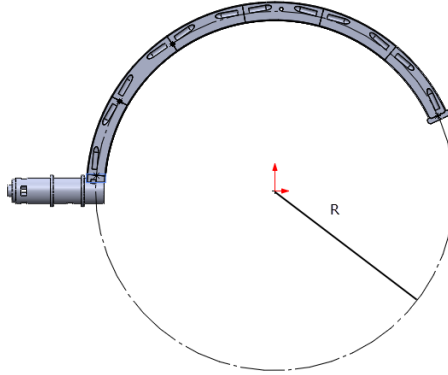
- The arm length l_2



- The nacelle radius l_3



- The arc radius R



- The suitable motor in term of capacity

For purpose of compactness, it has been decided that the arc radius (R) must be reduced as much as possible. So let it be $R = 0.315\text{m}$.

At first we have used Geogebra software to calculate approximately the kinematic chains lengths in order to cover the space needed to be travelled, the suitable choices founded are $l_1 = 0.09\text{m}$ and $l_2 = 0.16\text{m}$.

The choice of l_0 is very limited by the motors lengths as it is clear in 2.4.4, the length motor must not be significant otherwise the motors ends touch each other.

The choice of the motor was compelled by the torques must be provided to the mechanism. The torque must be provided to the mechanism can be calculated using the dynamic model (DM) established in the next chapter. Yet, the DM, itself depends on the mechanism dimensions which by their own are depending on the motor dimensions.

At first we start with the delta structure, The better way to know approximately the torque required, is to calculate a closed superior value for the torque. Ignoring the acceleration (for reasons mentioned in the next chapter), a closed superior torque is the torque provided for each forearm of the parallel structure to hold $1/3 \text{ kg}$ by each forearm end (this is because the weight of the end-effector is shared among the three motors), the torque is $(l_1 * 10/3 \approx 0.3 \text{ N.m})$. A suitable motor that can respect the geometric constraint on l_0 and provide more than 0.3N is the following Maxon assembly:

- Motor 1 name: Motor-DCX22L GB KL 18V
- Gear 1 name: Planetary gearhead-GPX26 C 231:1
- Encoder 1: Sensor-ENX16 EASY Absolute SSI



Figure 2.24: Maxon motor-gear

The same configuration is chosen for the fourth joint ψ , it is quite sufficient. For the fifth joint (ϕ), the following configuration is chosen:

- Motor 2 name: Motor-DCX32L GB KL 18V
- Gear 2 name: Planetary gearhead-GPX37 LZ 231:1
- Encoder 2: Sensor-ENX16 EASY Absolute SSI

The price of the first motor-gear type is : 407.83 Euro
 The price of the second motor-gear type is : 548.46 Euro
 The price of the associated controller : 416.62 Euro X 5



Figure 2.25: Maxon controller

The last point, that is worthy to be noted, is the benefit of introducing gears, having a reduction number of 231:1 and an absolute encoder of 1024 steps per turns, yields a total resolution of $360/(1024 * 231) = 0.000026 \text{ rad}$ for each motor. Regarding the tuned mechanism dimensions, the end-effector can travel in the space with an error less than $2.4 \mu\text{m}$ as long as there is no fabrication error.

Table of Mechanical and Electrical Parameters

Mechanical Parameters unit: m

l_0	l_1	l_2	l_3	R	R_p (Pulley radius)
0.8	0.09	0.16	0.8	0.315	$0.0377/2$

Electrical Parameters (unit: SI) .

Motor 1

R	L	K	J
0.68	$0.078 * 10^{-3}$	0.0146	$(9.82 + 1.8) * 10^{-7}$

Motor 2

R	L	K	J
0.165	$0.052 * 10^{-3}$	0.0195	$(75.9 + 11.9) * 10^{-7}$

Chapter 3

Modelling

Contents

3.1	Direct Geometric Model	36
3.1.1	The geometric model of the delta structure with respect to R_1	37
3.1.2	Transformation from R_1 to R_0	46
3.1.3	Validation	48
3.2	Inverse Geometric Model	49
3.2.1	Transformation from the vector P_0 to the vector P_1	49
3.2.2	The inverse geometric model of the parallel structure	50
3.2.3	A novel alternative IGM of the delta structure	50
3.2.4	Validation	56
3.3	Direct kinematic model	57
3.3.1	Validation	60
3.4	Inverse Kinematic Model	61
3.4.1	Validation	64
3.5	The Dynamic Model	65
3.5.1	The dynamic model of the delta structure	66
3.5.2	The dynamic model of the serial structure	71
3.5.3	Validation	73

3.1. DIRECT GEOMETRIC MODEL

The direct geometric model aims to calculate the end-effector coordinates (position and orientations) as a function of the joint variables of the mechanism ($\psi, \phi, \alpha_1, \alpha_2, \alpha_3$)[32].

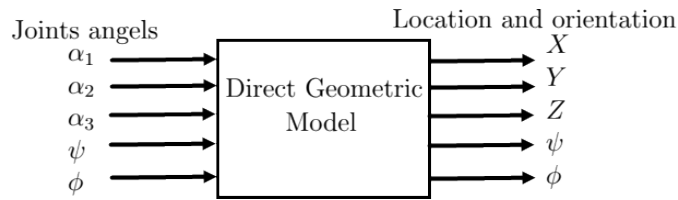


Figure 3.1: The geometric model input and output

The frames are assigned to the robot links in the way indicated bellow, so that the orientations angels of the end-effector are the same as the serial part joints angels (ψ, ϕ).

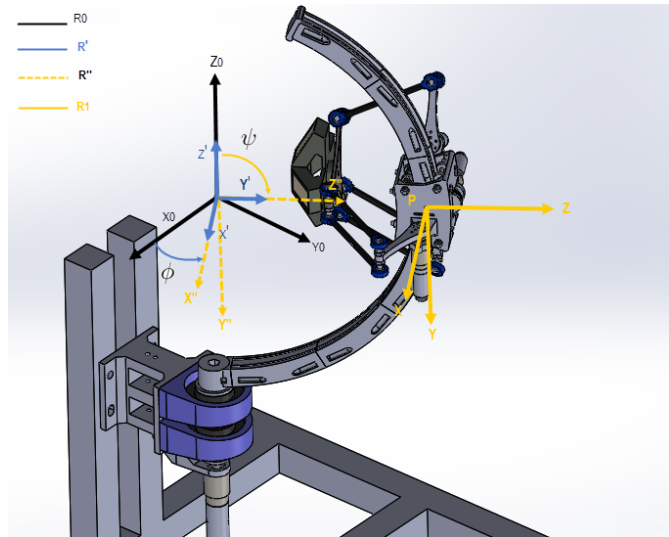


Figure 3.2: Transformations between frames

Having such a choice, we need just to find the end-effector position (X, Y, Z) as a function of $\psi, \phi, \alpha_1, \alpha_2$, and α_3 , in order to establish the DGM.
It is noticeable that the robot is composed of two main parts joined together in a serial chain :

- Serial part, which the joints are ψ and ϕ .
- A parallel structure which the joints are α_1 , α_2 , and α_3 .

In order to find the relationship between the joints angles and the end-effector Cartesian coordinates $P_{/R_0} = (X, Y, Z)$ with respect to the original frame R_0 , we must establish its Cartesian coordinates $P_{/R_1} = (x, y, z)$ with respect to the moving frame R_1 , as a function of α_1 , α_2 , and α_3 ; In the second step we project those calculated coordinates (x, y, z) into the steady frame R_0 , it is a transformation from R_1 to R_0 based on ψ and ϕ .

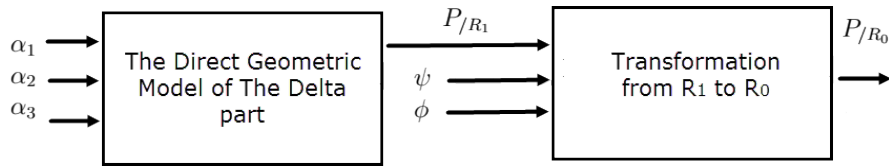


Figure 3.3: Direct geometric model of the hybrid robot

3.1.1. THE GEOMETRIC MODEL OF THE DELTA STRUCTURE WITH RESPECT TO R_1

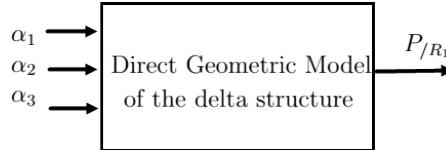


Figure 3.4: Direct geometric model of the delta structure R_i

Note: In this work, sometimes we refer to the end-effector expressions $P_{/R_0}$ and $P_{/R_1}$ by P_0 and P_1 , and the nacelle center position by P (with respect to R_1).

Unlike serial structures, for which the modeling is systematic and easy, modeling of closed chaine 'in this case delta structur', is no longer systematic, thus the systematic calculus (like Denavit-Hartenber mothode) is no longer available. The necessary organs to establish the geometric model for the delta structure are demonstrated bellow:

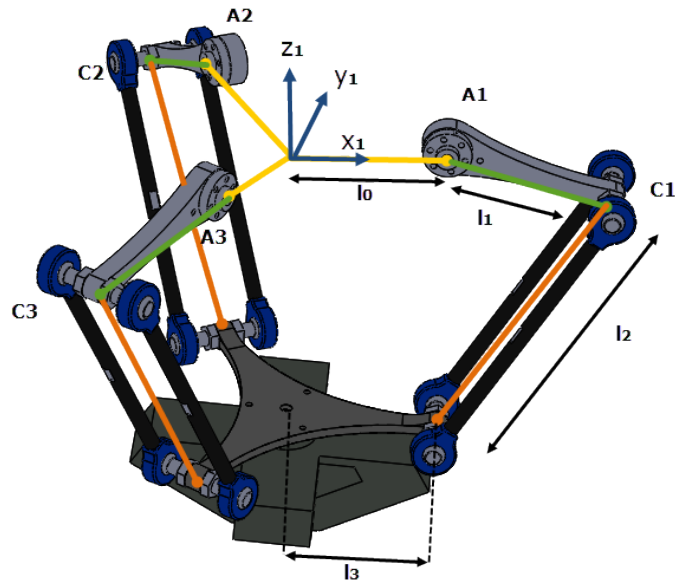


Figure 3.5: The kinematic chains

This structure can be simplified if we make a translation of each chain (segments l_1 and l_2) toward the axis Oz_1 by a distance of r (see the next figure).

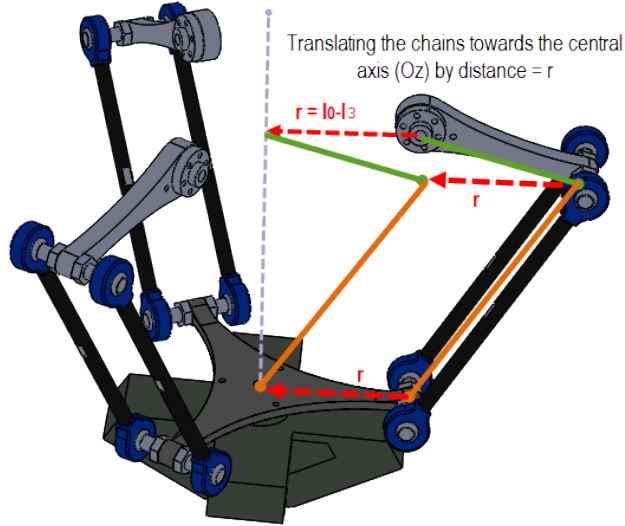


Figure 3.6: Translation of segments l_1 and l_2

we get this simplified geometric structure.

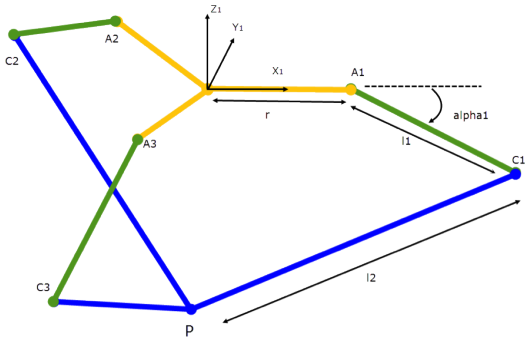


Figure 3.7: the simplified structure

Since we have $l_0 = l_3$ in this particular case, then $r = 0$; we get the following representation:

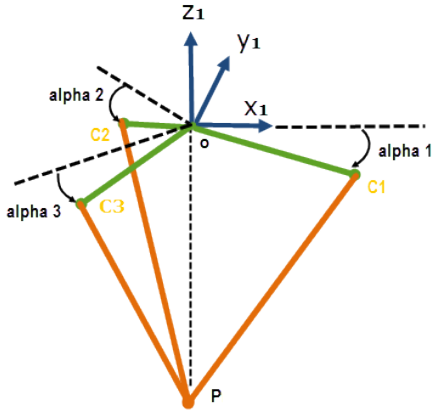


Figure 3.8: the simplified structure

Cartesian coordinates of C_1 , C_2 and C_3 with respect to R_1 :

We define two other coordinates systems R_2 and R_3 shifted from R_1 by rotations $\phi_2 = \frac{2\pi}{3}$ and $\phi_3 = \frac{4\pi}{3}$ respectively, around the axis (oz_1), see the next figure: 3.34. The rotation matrix from R_i to R_1 is defined as follows:

$$A_i = \begin{pmatrix} \cos(\phi_i) & -\sin(\phi_i) & 0 \\ \sin(\phi_i) & \cos(\phi_i) & 0 \\ 0 & 0 & 1 \end{pmatrix} \quad (3.1)$$

- The position of the point C_i :

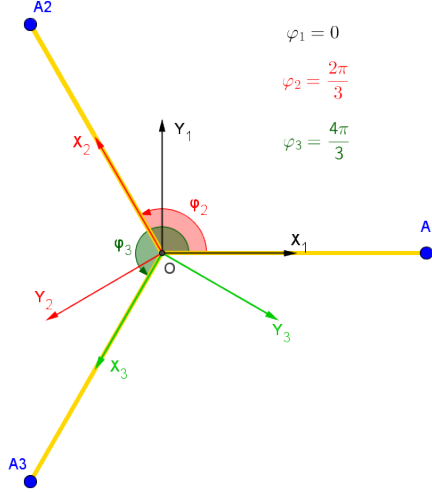


Figure 3.9: The different coordinates systems R_i

It is clear that, in R_i , the point C_i is positioned by the vector:

$$\overrightarrow{OC}_{i/Ri} = \begin{pmatrix} r + l_1 \cdot \cos(\phi_i) \\ 0 \\ -l_1 \cdot \sin(\phi_i) \end{pmatrix} \quad (3.2)$$

To find the coordinates of C_i with respect to frame R_1 , we just right-multiply the vector $\overrightarrow{OC}_{i/Ri}$ by the rotation matrix A_i , so we find:

$$\overrightarrow{OC}_i = A_i \cdot \overrightarrow{OC}_{i/Ri} = \begin{pmatrix} (r + l_1 \cdot \cos(\alpha_i)) \cos(\phi_i) \\ (r + l_1 \cdot \cos(\alpha_i)) \sin(\phi_i) \\ -l_1 \cdot \sin(\alpha_i) \end{pmatrix} \quad (3.3)$$

The next sections will show firstly Clavel model, then my proposed DGM.

Clavel formula for the delta structure DGM

It is clear that the three elbows C_1 , C_2 and C_3 belong to the same sphere ' S' surface, whose center is P and radius is l_2 , this method is developed by Clavel in his work.

The equations that define the sphere ' S' surface is the following:

$$(X_{c_i} - x)^2 + (Y_{c_i} - y)^2 + (Z_{c_i} - z)^2 = l_2^2 \quad (3.4)$$

with:

(x, y, z) : represents the coordinates of the point P with respect to R_1 .

$(X_{c_i}, Y_{c_i}, Z_{c_i})$: represent the coordinates of a point C_i belonging to the sphere ' S' surface.

As there are three points C_1, C_2 and C_3 , then there are three equations of three unknowns variables, it's a system of non-linear equations, that must be solved to find the nacelle position $P = (x, y, z)^T$ in term of α_1, α_2 and α_3 :

$$\begin{aligned}(X_{c_1} - x)^2 + (Y_{c_1} - y)^2 + (Z_{c_1} - z)^2 &= l_2^2 \\ (X_{c_2} - x)^2 + (Y_{c_2} - y)^2 + (Z_{c_2} - z)^2 &= l_2^2 \\ (X_{c_3} - x)^2 + (Y_{c_3} - y)^2 + (Z_{c_3} - z)^2 &= l_2^2\end{aligned}$$

Note that rather than to see the point P as a sphere center, it can also be seen as the intersection of three spheres of radius l_2 , centered in C_1, C_2 and C_3 , this vision guides us to the same equations established by Clavel.

This section will not elaborate the calculation steps to solve this equations system, in fact the method for solving such a system can be found in [Clavel], in which the solution is given as following:

$$D_1 = -l_2^2 + l_1^2 + r^2 + 2.r.l_1.\cos(\alpha_1)$$

$$D_2 = -l_2^2 + l_1^2 + r^2 + 2.r.l_1.\cos(\alpha_2)$$

$$D_3 = -l_2^2 + l_1^2 + r^2 + 2.r.l_1.\cos(\alpha_3)$$

$$E_1 = 2.(r + l_1.\cos(\alpha_1)).\cos(\phi_1)$$

$$E_2 = 2.(r + l_1.\cos(\alpha_2)).\cos(\phi_2)$$

$$E_3 = 2.(r + l_1.\cos(\alpha_3)).\cos(\phi_3)$$

$$F_1 = 2.(r + l_1.\cos(\alpha_1)).\sin(\phi_1)$$

$$F_2 = 2.(r + l_1.\cos(\alpha_3)).\sin(\phi_3)$$

$$F_3 = 2.(r + l_1.\cos(\alpha_3)).\sin(\phi_3)$$

$$G_1 = -2.l_1.\sin(\alpha_1)$$

$$G_2 = -2.l_1.\sin(\alpha_2)$$

$$G_3 = -2.l_1.\sin(\alpha_3)$$

$$H_1 = -(E_3 - E_1).(G_2 - G_1) + (G_3 - G_1).(E_2 - E_1)$$

$$H_2 = -(F_3 - F_1).(E_2 - E_1) + (E_3 - E_1).(F_2 - F_1)$$

$$H_3 = -(D_3 - D_1).(E_2 - E_1) + (E_3 - E_1).(D_2 - D_1)$$

$$H_4 = (D_3 - D_1).(F_2 - F_1) + (F_3 - F_1).(D_1 - D_2)$$

$$H_5 = -(G_3 - G_1).(F_2 - F_1) - (F_3 - F_1).(G_1 - G_2)$$

$$L = 1 + (H_5^2 + H_1^2)/H_2^2$$

$$M = -2.(H_5 \cdot H_4 + H_1 \cdot H_3)/H_2^2 + (E_1 \cdot H_5 + F_1 \cdot H_1)/H_2 + G_1$$

$$N = D_1 + (H_4^2 + H_3^2)/H_2^2 - (E_1 \cdot H_4 + F_1 \cdot H_3)/H_2$$

Given that, the coordinates of the nacelle center with respect to R_1 are:

$$z = \frac{M - \sqrt{(M^2 - 4 \cdot L \cdot N)}}{2 \cdot L}$$

$$x = \frac{H_5 \cdot z + H_4}{H_2}$$

$$y = \frac{H_1 \cdot z + H_3}{H_2}$$

A novel formula for the DGM of the delta structure

The study of closed-chain robots is specific to each structure, here where one may find different visions or solutions for the same structure. However, to avoid complicated calculus, the delta structure should be seen differently.

By observing the delta structure, we can notice that the isosceles pyramid defined by its triangular base (C_1, C_2, C_3), and its vertex P , has an interesting features that may be a shortcut to the solution (see the next figure 3.10).

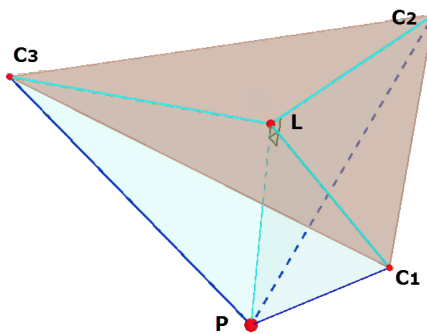


Figure 3.10: The Isosceles pyramid $C_1C_2C_3P$

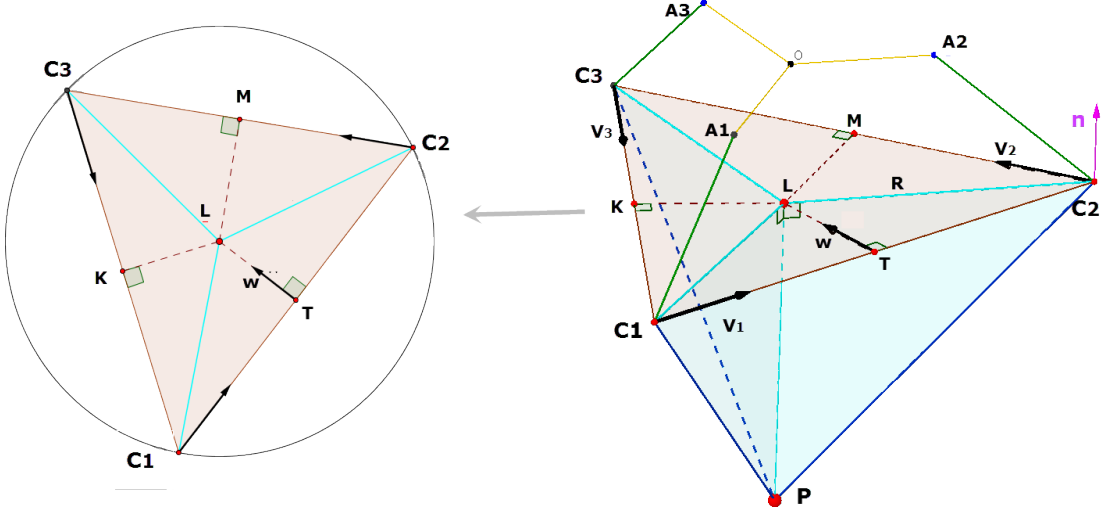


Figure 3.11: Representation of objects used in DGM

The point L , which is the projection of the point P onto the plane $(C_1C_2C_3)$, is coincident with the center of the circle passing through these three points (circumscribed circle). In fact the three triangles C_1LP , C_2LP and C_3LP are congruent, this is because they have: three equal segments $C_1P = C_2P = C_3P = l_2$; a common segment LP ; and three equal angles (they are equal because L represents the projection of P onto the plane $(C_1C_2C_3)$, so the segment LP is perpendicular to each segment belonging to this plane). Therefore, we can conclude that $C_1L = C_2L = C_3L$. The point L thereupon represents the center of the circumcircle of the triangle $C_1C_2C_3$. Its circumradius verifies : $R = C_1L = C_2L = C_3L$.

It is clear that $\overrightarrow{OP} = \overrightarrow{OT} + \overrightarrow{TL} + \overrightarrow{LP}$.
 (see the figure 3.11 in the next page 43)
 Before to continue, we define the following parameters :

$$a = |\overrightarrow{C_1C_2}| \quad b = |\overrightarrow{C_2C_3}| \quad c = |\overrightarrow{C_3C_1}| \quad (3.5)$$

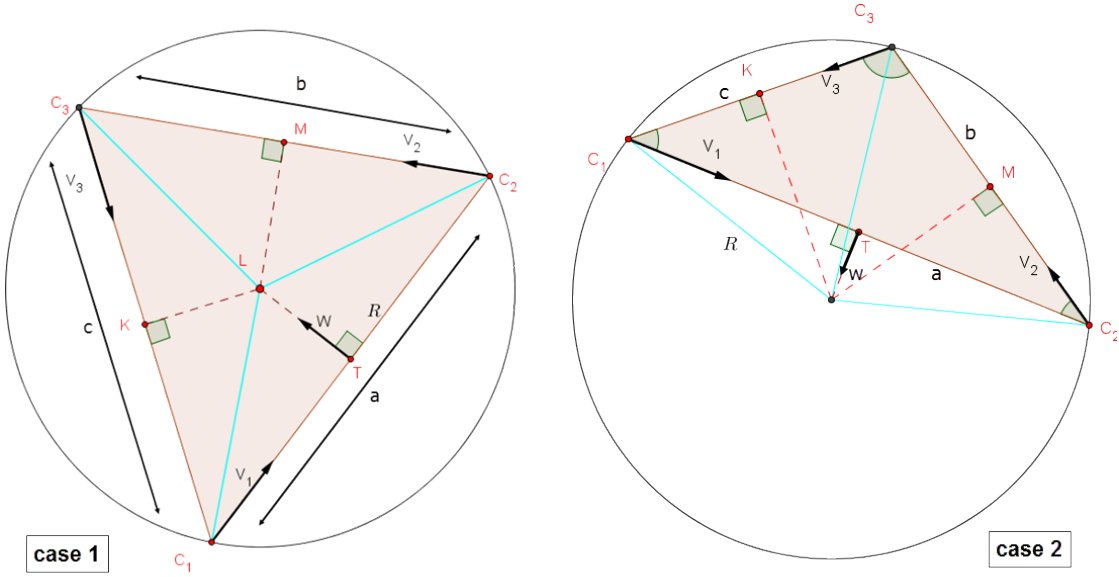
$$\overrightarrow{V}_1 = \frac{\overrightarrow{C_1C_2}}{a}, \quad \overrightarrow{V}_2 = \frac{\overrightarrow{C_2C_3}}{a}, \quad \overrightarrow{V}_3 = \frac{\overrightarrow{C_3C_1}}{a} \quad (3.6)$$

In this part of modeling we just need \overrightarrow{V}_1 , by the time the two others are required in the next parties.

The vector \overrightarrow{OT} is calculated as following :

$$\overrightarrow{OT} = \frac{\overrightarrow{OC_1} + \overrightarrow{OC_2}}{2}$$

(3.7)


 Figure 3.12: direction of the unit vector ω

$$\overrightarrow{TL} = TL \cdot \overrightarrow{\omega} \quad (3.8)$$

we must calculate TL and $\overrightarrow{\omega}$, so let be the following vector : $\overrightarrow{S} = \overrightarrow{C_3C_1} \wedge \overrightarrow{C_1C_2}$. it is a normal vector to the plane $(C_1C_2C_3)$, on the other hand $\overrightarrow{S} = S \cdot \overrightarrow{n}$, where S represents two times the surface of the triangle $C_1C_2C_3$ and \overrightarrow{n} is the unit normal vector thereof.

S is calculated by the following formula :

$2.R.S = a.b.c$. R : is the circumradius of the circumscribed circle passing through $(C_1C_2C_3)$, it is therefrom calculated as following :

$$R = \frac{a.b.c}{\sqrt{p(p-2a)(p-2b)(p-2c)}} \quad (3.9)$$

where $p = a + b + c$

Next, in order to obtain $\overrightarrow{\omega}$ we distinguish two cases as it is illustrated in the figure 3.12.

- In the first case we have: $\overrightarrow{\omega} = \overrightarrow{n} \wedge \overrightarrow{V_1}$.
- In the second case we have: $-\overrightarrow{\omega} = \overrightarrow{n} \wedge \overrightarrow{V_1}$.

In fact, in the first case we find $\widehat{C_1C_2C_3} < \frac{\pi}{2}$

and we have accordingly to El-Kashi's relation: $a^2 = b^2 + c^2 - 2.b.c.\cos(\widehat{C_1C_2C_3})$

Thus: $a^2 < b^2 + c^2$.

In the second case: $C_1\widehat{C_2C_3} < \frac{\pi}{2}$

So : $a^2 > b^2 + c^2$.

We conclude that :

$$\vec{\omega} = sign(b^2 + c^2 - a^2) \cdot \vec{n} \wedge \vec{V}_1 \quad (3.10)$$

it remains to calculate TL .

In the right triangle C_2TL :

$$TL = \sqrt{R^2 - \left(\frac{a}{2}\right)^2} \quad (3.11)$$

Also we have:

$$\vec{LP} = -LP \cdot \vec{n} \quad (3.12)$$

Where, in the right triangle C_1LP :

$$LP = \sqrt{l_2^2 - R^2} \quad (3.13)$$

At this point, the calculus of $P = (x, y, z)$ is finished, it remains just one thing. In returning to the definitions of parameters, we notice that V_1 (resp V_2, V_3) is no longer defined when a comes null (resp V_2, V_3 are nulls), It yields that there is three singularity's cases : $(C_1, C_2) \in (oz)$, or $(C_1, C_2) \in (oy)$ or $(C_1, C_2) \in (ox)$ i.e. if there is two points belonging to the same axis (oz) (for example C_2 and C_3), then, even if the third point (for the ex-example : C_1) is fixed, the point P can take any position located in a circle centered in the middle point of its normal segment-line C_3C_1 ($C_2 = C_3$), its radius equals to $r = \sqrt{l_2^2 - \left(\frac{C_3C_1}{2}\right)^2}$. Furthermore it can move on sphere surface , if all of theme belong to (oz) .

The Attractive point coordinates with respect to R_1

The actuator carried by the nacelle generates a stable attractive point (the end-effector point which is referred to as P_0 and P_1) at a distance of L from the nacelle center P :

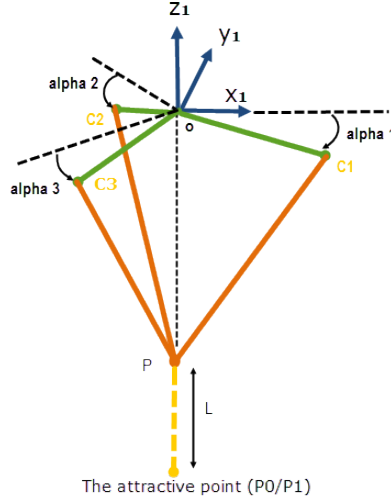


Figure 3.13: The controlled point (the attractive point)

Thus:

$$P_1 = P + (0, 0, -L)^T_{/R_1} \quad (3.14)$$

At this point, all what we need, in order to accomplish the direct geometric modeling, is to find the expression of the point P in the global reference R_0 .

3.1.2. TRANSFORMATION FROM R_1 TO R_0

This part represents the direct geometric model of serial part of the mechanism, in which we must describe the relationship between the frame R_0 and R_1 .

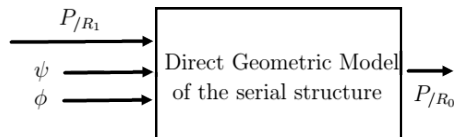


Figure 3.14: Direct geometric model of the serial part

This transformation (translation and orientation from frame R_0 into frame R_1) can be defined by *the homogeneous transformation* represented by the matrix T_0^1 denoted as:

$$T_0^1 = \begin{bmatrix} A''_0 & P''_1 \\ 0 & 1 \end{bmatrix}$$

A''_0 represents the orientation matrix from R_0 to R'' , while P''_1 is the origin coordinates of R_1 with respect to R'' . T_0^1 can be calculated automatically using

systematic method like *Denavit and Hartenberg* or *W Khalil ,and E Dombre [Khalil]*. This transformation is composed of three successive transformations as it is demonstrated in the next figure:

- Orientation from frame R_0 to frame R' around $z - axis$ by an angle ϕ .
- Orientation from frame R' to frame R'' around $ox' - axis$ by an angle ψ .
- Translation from frame R'' to frame R_1 through $oy'' - axis$ by distance R .

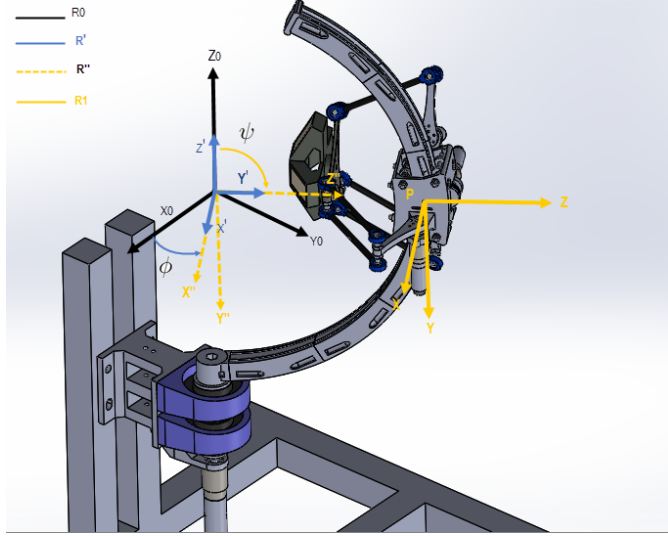


Figure 3.15: Transformations between frames

Translation from frame R'' to frame R_1 is represented by the vector P''_1 which represents the Cartesian coordinates of the frame R_1 origin with respect to frame R'' :

$$P''_1 = \begin{pmatrix} 0 \\ 0 \\ R \end{pmatrix} \quad (3.15)$$

The orientation from frame R_0 to frame R'' is represented by the matrix A''_0 and it can be easily calculated:

$$A''_0 = \begin{pmatrix} \cos(\phi) & -\cos(\psi).\sin(\phi) & -\sin(\psi).\sin(\phi) \\ \sin(\phi) & \cos(\psi).\cos(\phi) & \sin(\psi).\cos(\phi) \\ 0 & -\sin(\psi) & \cos(\psi) \end{pmatrix} \quad (3.16)$$

Finally :

$$P_0 = A''_0.(P_1 + P''_1) \quad (3.17)$$

At this point the direct geometric model is accomplished.

3.1.3. VALIDATION

Using the model exported from SolidWorks environment to SimMechanics environment we test whether‘ the analytic DGM is accurate or not:

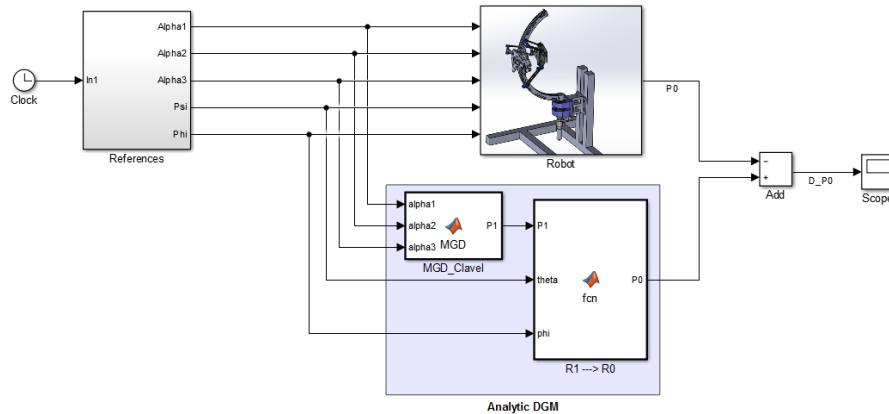


Figure 3.16: Simulink diagram to validate the DGM

The scope shows the difference between two signals represent the end-effector position X, Y, Z with respect to frame R_0 , one signal is from the block named *Robot* representing the model imported from SolidWorks environment, and the other comes from the block named *Analytic DGM* representing the model calculated in this section. Both diagrams receive their inputs from the same source; the result of the simulation is illustrated bellow:

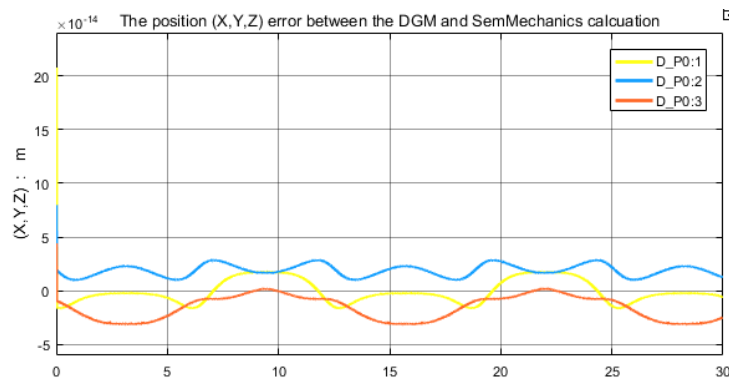


Figure 3.17: The error of the DGM

The simulation shows that DGM is very accurate since the error order is 10^{-14} . The DGM elaborated in this section is valid.

3.2. INVERSE GEOMETRIC MODEL

The Inverse Geometric model gives us the joint angles $\alpha_1, \alpha_2, \alpha_3, \psi$, and ϕ as a function of orientation and location (X, Y, Z) of the end-effector.

As mentioned in the DGM section, the end-effector orientations are the same as the serial part joint angles ψ , and ϕ , thus the objective of this section is to calculate $\alpha_1, \alpha_2, \alpha_3$ in term of $(X, Y, Z), \psi$, and ϕ .

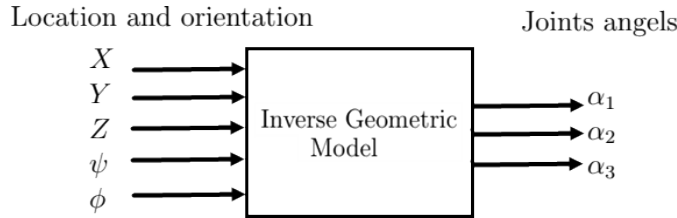


Figure 3.18: Inverse Geometric Model inputs and outputs

Since the structure of the robot is composed mainly of two parts: serial one and parallel one, then we will proceed to find at first the end-effector coordinates P_1 with respect to R_1 in term of P_0, ψ , and ϕ , and in the second step the joint angles α_1, α_2 , and α_3 are established in term of P_1 :

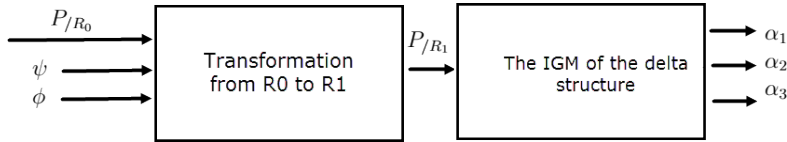


Figure 3.19: Inverse Geometric Model inputs and outputs

3.2.1. TRANSFORMATION FROM THE VECTOR P_0 TO THE VECTOR P_1

The transformation from P_{R0} to P_{R1} can be calculated easily by following the opposite steps indicated in the DGM. Nevertheless, it can be also established in a straight way from the equation 3.17:

$$P_0 = A''_0 \cdot (P_1 + P''_1) \quad (3.18)$$

It yields that:

$$P_1 = A''_0^{-1} \cdot P_0 - P''_1 \quad (3.19)$$

Notice that $A_0''^{-1} = A_0''^T$, due the fact that A_0'' is an orientation matrix between two orthonormal Cartesian coordinates systems.

3.2.2. THE INVERSE GEOMETRIC MODEL OF THE PARALLEL STRUCTURE

This section aims to find the necessary angles to reach a specific position of the end-effector with respect to the frame R_1 ,

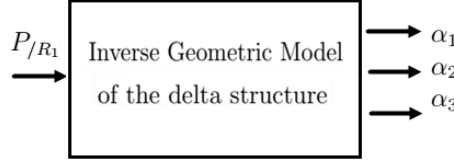


Figure 3.20: Inverse Geometric Model of the parallel structure

Multiple formulations have been proposed in order to calculated the inverse geometric model of the delta robot [30], [33].

The IGM can be established by resolving the equations in the DGM, this solution has been proposed by Clavel [30] as following:

$$\alpha_i = \text{atang} \left(\frac{-2z + \sqrt{4z^2 + 4r^2 - S^2 + Q_i^2(1 - \frac{r^2}{l_1^2}) + Q_i(-2\frac{rS}{l_1} - 4r)}}{-2r - S - Q_i(\frac{r}{l_1} - 1)} \right) \quad (3.20)$$

Where :

$$Q_i = 2.x.\cos(\phi_i) + 2.y.\sin(\phi_i) \quad (3.21)$$

$$S = \frac{1}{l_1} (-x^2 - y^2 - z^2 + l_2^2 - l_1^2 - r^2) \quad (3.22)$$

3.2.3. A NOVEL ALTERNATIVE IGM OF THE DELTA STRUCTURE

1. introduction according to the figure below, we notice that C_i represents one of tow intersections of the circle K_i , whose radius is l_1 , and center is $(r, 0, 0)_{R_i}$, with the sphere (S) , whose radius is l_2 , and centered in P' .

In order to simplify the problem , we will not determine those intersection

(C_i and C'_i) directly, but by noticing the sphere (S) intersects the plane (ox_iz_i) in the circle K'_i , which itself intersects with K_i making two points, C_i is one of them.

2. Determination of the circle K'_i (radius and center) :

According to the following figure, to determine the center of K'_i , it is sufficient to project P_i onto the plane ox_iz_i , see the figure 3.21.

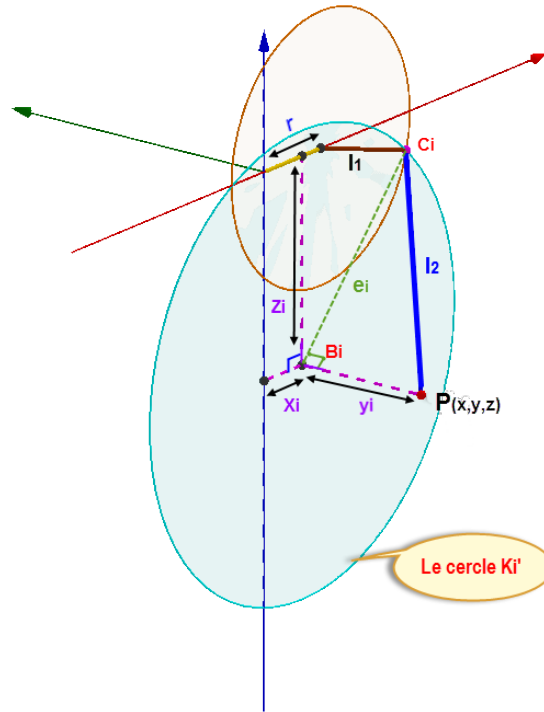


Figure 3.21: The projection of P onto the plane ox_iz_i

P_i represents the coordinates of the point P in R_i , so in the plane (ox_iz_i), the point P_i has the following coordinates:

$$P_i = \begin{pmatrix} x_i \\ y_i \\ z_i \end{pmatrix} = \begin{pmatrix} \cos\phi_i & \sin\phi_i & 0 \\ -\sin\phi_i & \cos\phi_i & 0 \\ 0 & 0 & 1 \end{pmatrix} \cdot P \quad (3.23)$$

It remains to determine the radius e_i of K'_i , since B_i is the projection of the point P onto the plane (ox_iz_i) 'figure 3.21', the triangle $C_iP_iB_i$ is right angled at B_i , it is determined by l_2 and $|y_i|$, thus :

$$e_i = \sqrt{l_2^2 - y_i^2} \quad (3.24)$$

3. Determination of α_i :

In the plane $(ox_i z_i)$ (see the figure 3.22), the circle K_i intersects with K'_i in two points (C_i and C'_i) corresponding respectively to α_i and α'_i .

The two triangles $A_i C_i P_i$ and $A_i C'_i P_i$ are symmetrical around a common segment line $A_i P_i$ which makes an angle β_i with the axis (ox_i) , if we know β_i , it will be sufficient to know δ_i , in order to determine α_i and α'_i i.e :

$$\boxed{\alpha_i = \beta_i - \delta_i \quad ; \quad \alpha'_i = \beta_i + \delta_i} \quad (3.25)$$

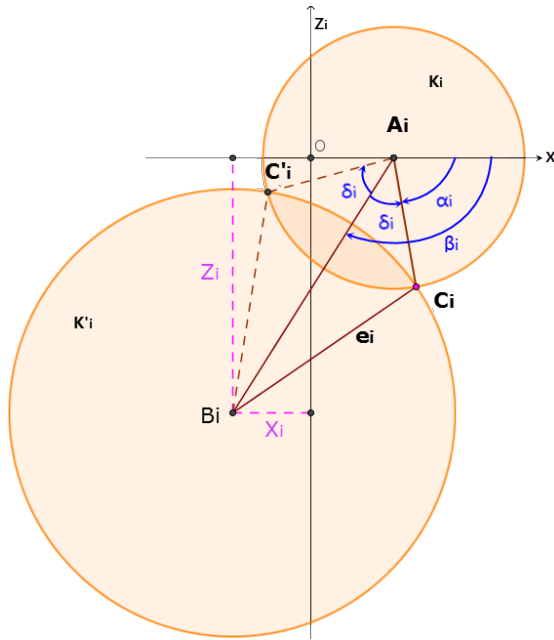


Figure 3.22: The intersection of K_i with K'_i

 (a) Calculus of β_i :

according to the previous figure, the angle β_i is resulted from the intersection of the axis (ox_i) with the segment $A_i B_i$:

$$\tan(\beta_i) = \frac{-z_i}{x_i - r} \quad (3.26)$$

The negative sign has appeared because $\tan(\beta_i)$ is positive in the first quadrant, meanwhile z is negative therein, which is followed from the fact that it is oriented into the opposite sense of the conventional sense. Note. β_i is no longer defined when $z_i = (x_i - r) = 0$, we will deal with

it later, so according to the figure 3.23 , β_i is defined as:

$$\boxed{\beta_i = \text{atan}2(-z_i, x_i - r)} \quad (3.27)$$

i.e :

$$\beta_i = \begin{cases} \text{atan} \left(\frac{-z_i}{x_i - r} \right) & \text{if } (x_i - r) > 0 \\ \text{atan} \left(\frac{-z_i}{x_i - r} \right) + \pi & \text{if } (x_i - r) < 0 \\ \frac{\pi}{2} & \text{if } (x_i - r) < 0 \text{ and } -z_i > 0 \\ -\frac{\pi}{2} & \text{if } (x_i - r) < 0 \text{ and } -z_i < 0 \\ \text{not defined} & \text{if } x_i - r = 0 \\ & \text{and } z_i = 0 \end{cases} \quad (3.28)$$

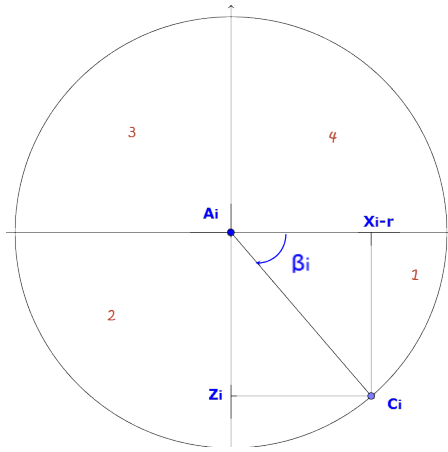


Figure 3.23: The angle β_i sense

(b) Calculus of δ_i :

In the triangle $A_iB_iC_i$, which is defined by three segment-lines A_iB_i , e_i and l_2 .

we apply the theorem of El-Kashi as follows :

$$\boxed{e^2 = l_2^2 + A_iB_i^2 - 2l_2A_iB_i \cos\delta_i} \quad (3.29)$$

$$\Rightarrow \cos\delta_i = \frac{l_2^2 + A_iB_i^2 - e^2}{2l_2A_iB_i}$$

$$\Rightarrow \delta_i = \arccos \left(\frac{l_2^2 + A_iB_i^2 - e^2}{2l_2A_iB_i} \right) \quad (3.30)$$

where:

$$A_i B_i = \sqrt{z_i^2 + (x_i - r)^2} \quad (3.31)$$

4. The singularity points:

Now, we will discuss the case where β_i is not defined, β_i is no longer defined if both $x_i - r$ and z_i are null, but what does it mean when both of them are null in the same time ?

It means that the projection of the point P onto the plane ($ox_i z_i$) coincides with the center of K_i (i.e: the point A_i), whence the end-effector P , in this case, is located in the line which is parallel to the axis (oy_i) and passing through A_i , see the next figure.

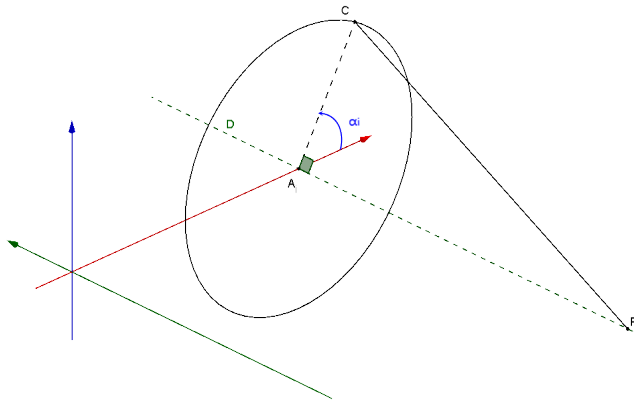


Figure 3.24: A_i is the projection of P , when it is a singularity point

It should be noted also, that the triangle $A_i C_i P$ has a right angle at A_i , thus:

$$|y_i| = \sqrt{l_2^2 - l_1^2} \implies y_i = \pm \sqrt{l_2^2 - l_1^2} \quad (3.32)$$

So β_i is no longer defined for this following points:

$$P_{i1} = \begin{pmatrix} r \\ \sqrt{l_2^2 - l_1^2} \\ 0 \end{pmatrix}, \quad P_{i2} \begin{pmatrix} r \\ -\sqrt{l_2^2 - l_1^2} \\ 0 \end{pmatrix} \quad (3.33)$$

This two points are expressed in the coordinates system R_i , so, to express them in R_0 , it is sufficient to multiply them by :

$$A_i = \begin{pmatrix} \cos\phi_i & -\sin\phi_i & 0 \\ \sin\phi_i & \cos\phi_i & 0 \\ 0 & 0 & 1 \end{pmatrix}, \quad P_{i/R_i} = A_i \cdot P_{i/R_i}$$

Also we obtain :

$$P_{i1/R_1} = \begin{pmatrix} r \cos \phi_i \\ \sqrt{l_2^2 - l_1^2} \sin \phi_i \\ 0 \end{pmatrix} \quad (3.34)$$

$$P_{i2/R_1} = \begin{pmatrix} r \cos \phi_i \\ -\sqrt{l_2^2 - l_1^2} \sin \phi_i \\ 0 \end{pmatrix} \quad (3.35)$$

Note :

For each angle α_i we find two symmetrical points of singularity P_{i1} and P_{i2} , one of them in the positive sense of (oy_i) , and the other in the negative sense. Finally we have 6 points of singularity, which all of them are located in the plane (oxy) as following:

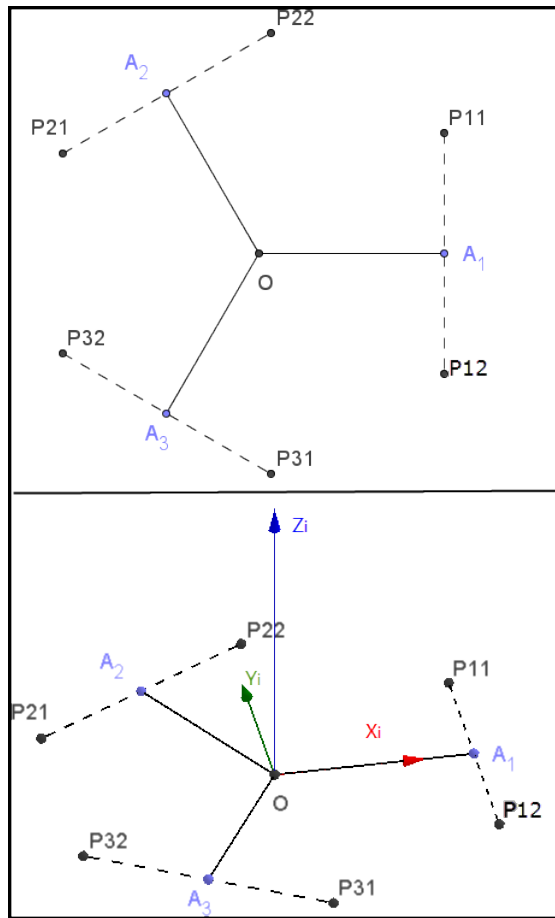


Figure 3.25: Singularity points

These points of singularity do not affect. In fact the robot cannot reach those points due to the mechanical limitation.

3.2.4. VALIDATION

Using the model exported from SolidWorks environment to SimMechanics environment we test whether the the analytic IGM is accurate or not:

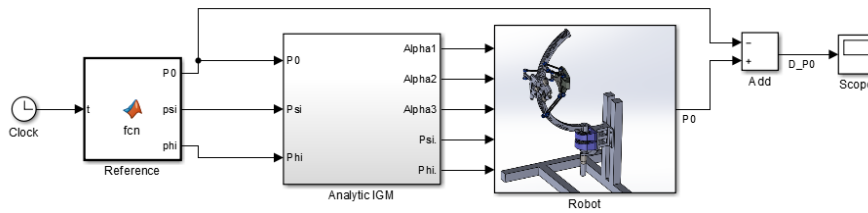


Figure 3.26: Simulink diagram to validate the DGM

This time the validation of the model is concluded implicitly, because it is not possible to use the model imported from SolidWorks environment as an IGM.

The scope shows the difference between two signals represent the end-effector position X, Y, Z , one signal is from the block named *Robot* representing the model imported, and the other comes out from the reference block, between these two blocks the IGM is placed. The point of the this implicit conclusion is that the DGM is bijective function, which would give a different output than the reference if the IGM was incorrect.

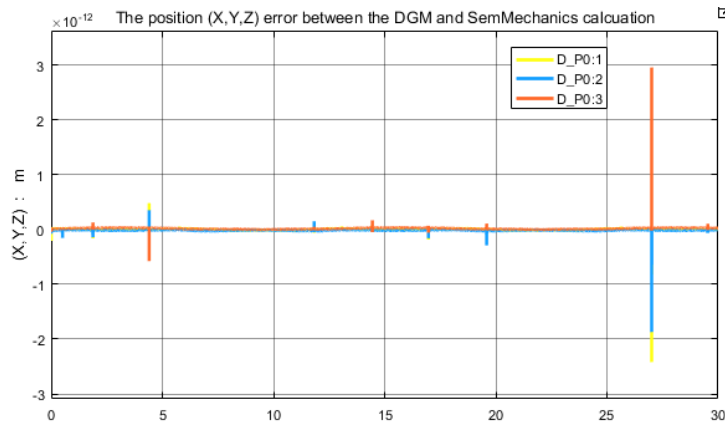


Figure 3.27: The error of the DGM

The simulation shows that IGM is very accurate since the error order is 10^{-12} , the DGM elaborated in this section is valid.

3.3. DIRECT KINEMATIC MODEL

After having obtained the DGM, we will derive it to determine the direct kinematic model (DKM), which gives the velocity of the end effector in term of the joints angular velocities $\dot{\alpha}_i$, $\dot{\psi}$, and $\dot{\phi}$

The position of the end-effector is a function of the joint angles

$$P_0 = F(\alpha_1, \alpha_2, \alpha_3, \psi, \phi) = \begin{pmatrix} F_x(\alpha_1, \alpha_2, \alpha_3, \psi, \phi) \\ F_y(\alpha_1, \alpha_2, \alpha_3, \psi, \phi) \\ F_z(\alpha_1, \alpha_2, \alpha_3, \psi, \phi) \end{pmatrix} \quad (3.36)$$

And the velocity is calculated as following :

$$\frac{dP_0}{dt} = \begin{pmatrix} \frac{\partial F_x}{\partial \alpha_1} & \frac{\partial F_x}{\partial \alpha_2} & \frac{\partial F_x}{\partial \alpha_3} & \frac{\partial F_x}{\partial \psi} & \frac{\partial F_x}{\partial \phi} \\ \frac{\partial F_y}{\partial \alpha_1} & \frac{\partial F_y}{\partial \alpha_2} & \frac{\partial F_y}{\partial \alpha_3} & \frac{\partial F_y}{\partial \psi} & \frac{\partial F_y}{\partial \phi} \\ \frac{\partial F_z}{\partial \alpha_1} & \frac{\partial F_z}{\partial \alpha_2} & \frac{\partial F_z}{\partial \alpha_3} & \frac{\partial F_z}{\partial \psi} & \frac{\partial F_z}{\partial \phi} \end{pmatrix} \cdot \begin{pmatrix} \frac{d\alpha_1}{dt} \\ \frac{d\alpha_2}{dt} \\ \frac{d\alpha_3}{dt} \\ \frac{d\psi}{dt} \\ \frac{d\phi}{dt} \end{pmatrix} \quad (3.37)$$

The partial derivation can be calculated numerically.

However, given the alternative DGM we proposed, it is easy to turn out analytically the DKM form it. Returning back to the equation:

$$P_{/R_0} = A''_0 (P_{/R_1} + P''_1) \quad (3.38)$$

where

$$P_{/R_1} = P_{n/R_1} + (0, 0, -L)^T \quad (3.39)$$

By derivation, the DGM is defined by the following equation:

$$\boxed{\dot{P}_{/R_0} = \dot{A''}_0 (P_{/R_1} + P''_1) + A''_0 \dot{P}_{/R_1}} \quad (3.40)$$

Calculation of \dot{A}_0''

we have found that :

$$\overrightarrow{OP} = \overrightarrow{OT} + \overrightarrow{TL} + \overrightarrow{LP} \implies \dot{\overrightarrow{OP}} = \dot{\overrightarrow{OT}} + \dot{\overrightarrow{TL}} + \dot{\overrightarrow{LP}} \quad (3.41)$$

Befor to continue let us calculate the following derivatives :

1. Calculus of $\dot{\overrightarrow{OC_i}}$:

$$\dot{\overrightarrow{OC_i}} = \begin{pmatrix} -l_1 \cdot \sin(\alpha_i) \cdot \cos(\phi_i) \\ -l_1 \cdot \sin(\alpha_i) \cdot \sin(\phi_i) \\ -l_1 \cdot \cos(\alpha_i) \end{pmatrix} \cdot \dot{\alpha_i} \quad (3.42)$$

2. Derivatives of the lengths a , b and c :

$$a^2 = \overrightarrow{C_1 C_2} \cdot \overrightarrow{C_1 C_2} \quad (3.43)$$

which implies :

$$2a\dot{a} = \overrightarrow{C_1 C_2} \cdot \dot{\overrightarrow{C_1 C_2}} + \dot{\overrightarrow{C_1 C_2}} \cdot \overrightarrow{C_1 C_2} = 2 \cdot \overrightarrow{C_1 C_2} \cdot \dot{\overrightarrow{C_1 C_2}} \quad (3.44)$$

$$\implies \dot{a} = \frac{\overrightarrow{C_1 C_2} \cdot \dot{\overrightarrow{C_1 C_2}}}{a} \quad (3.45)$$

$$\dot{a} = \overrightarrow{V_1} \cdot \dot{\overrightarrow{C_1 C_2}} \quad (3.46)$$

Also we find :

$$\dot{b} = \overrightarrow{V_2} \cdot \dot{\overrightarrow{C_2 C_3}} \quad et \quad \dot{c} = \overrightarrow{V_3} \cdot \dot{\overrightarrow{C_3 C_1}} \quad (3.47)$$

where : $\dot{\overrightarrow{C_i C_j}} = \dot{\overrightarrow{OC_j}} - \dot{\overrightarrow{OC_i}}$

3. The derivative of the unit vector V_1 :

$$\overrightarrow{C_1 C_2} = a \cdot \overrightarrow{V_1} \implies \dot{\overrightarrow{C_1 C_2}} = a \cdot \dot{\overrightarrow{V_1}} + \dot{a} \cdot \overrightarrow{V_1} \implies \dot{\overrightarrow{V_1}} = \frac{\dot{\overrightarrow{C_1 C_2}} - \dot{a} \cdot \overrightarrow{V_1}}{a} \quad (3.48)$$

4. Calculus of $\dot{\vec{n}}$ and $\dot{\vec{\omega}}$:

We have seen that $\dot{\vec{S}} = \overrightarrow{C_3 C_1} \wedge \overrightarrow{C_1 C_2}$

which means

$$\dot{\vec{S}} = \dot{\overrightarrow{C_3 C_1}} \wedge \overrightarrow{C_1 C_2} + \overrightarrow{C_3 C_1} \wedge \dot{\overrightarrow{C_1 C_2}} \quad (3.49)$$

On the other hand: $\vec{S} = S \cdot \vec{n}$

Hence:

$$\dot{\vec{S}} = \dot{S} \cdot \vec{n} + S \cdot \dot{\vec{n}} \implies \dot{\vec{n}} = \frac{(\dot{\vec{S}} - \dot{S} \cdot \vec{n})}{S} \quad (3.50)$$

The a new term \dot{S} will be calculated later.

Also we have:

$$\begin{aligned} \vec{\omega} &= \text{sign}(b^2 + c^2 - a^2) \cdot (\vec{n} \wedge \vec{V}_1) \\ \implies \vec{\omega} &= \text{sign}(b^2 + c^2 - a^2) (\dot{\vec{n}} \wedge \vec{V}_1 + \vec{n} \wedge \dot{\vec{V}}_1) \end{aligned}$$

5. calculus of \dot{R} :

we know that :

$$R = \frac{a \cdot b \cdot c}{\sqrt{p(p-2a)(p-2b)(p-2c)}} , \quad p = a + b + c \quad (3.51)$$

This equation can be linearized by the logarithmic function :

$$\begin{aligned} \ln(R) &= \ln(a) + \ln(b) + \ln(c) - \\ &\quad \frac{1}{2} (\ln(p) + \ln(p-2a) + \ln(p-2b) + \ln(p-2c)) \end{aligned} \quad (3.52)$$

Now, it is more easier to derive it:

$$\dot{R} = \left(\frac{\dot{a}}{a} + \frac{\dot{b}}{b} + \frac{\dot{c}}{c} - \frac{1}{2} \left[\frac{\dot{p}}{p} + \frac{\dot{p}-2\dot{a}}{p-2a} + \frac{\dot{p}-2\dot{b}}{p-2b} + \frac{\dot{p}-2\dot{c}}{p-2c} \right] \right) \cdot R \quad (3.53)$$

where :

$$ML = \sqrt{R^2 - \frac{b^2}{4}} \quad \text{and} \quad KL = \sqrt{R^2 - \frac{c^2}{4}}$$

6. calculus of \dot{S} :

We have seen that $2 \cdot R \cdot S = a \cdot b \cdot c$, by linearizing this equation with \ln function we find: $\ln(2) + \ln(R) + \ln(S) = \ln(a) + \ln(b) + \ln(c)$, then we derive it:

$$\dot{S} = \left(\frac{\dot{a}}{a} + \frac{\dot{b}}{b} + \frac{\dot{c}}{c} - \frac{\dot{R}}{R} \right) \cdot S \quad (3.54)$$

7. Calculus of $\dot{\vec{OT}}$:

$$\dot{\vec{OT}} = \frac{\dot{\vec{OC}_1} + \dot{\vec{OC}_2}}{2} \quad (3.55)$$

8. Calculus of $\dot{\overrightarrow{TL}}$:

$$\text{since } TL^2 = R^2 - \frac{a^2}{4}$$

$$\text{then } TL \cdot \dot{TL} = R \cdot \dot{R} - \frac{a\dot{a}}{4}$$

$$\dot{TL} = \left(R \cdot \dot{R} - \frac{a\dot{a}}{4} \right) \frac{1}{TL} \quad (3.56)$$

$$\dot{\overrightarrow{TL}} = \dot{TL} \cdot \vec{\omega} + TL \cdot \dot{\vec{\omega}} \quad (3.57)$$

9. calculus of $\dot{\overrightarrow{LP}}$:

$$\dot{\overrightarrow{LP}} = -\dot{LP} \cdot \vec{n} - LP \cdot \dot{\vec{n}} \quad (3.58)$$

$\dot{\vec{n}}$ has been calculated , it remains \dot{LP}

$$LP^2 = l_2^2 - R^2 \implies \dot{LP} = \frac{-R \cdot \dot{R}}{LP} \quad (3.59)$$

3.3.1. VALIDATION

The simulation demonstrates the validity of the model:

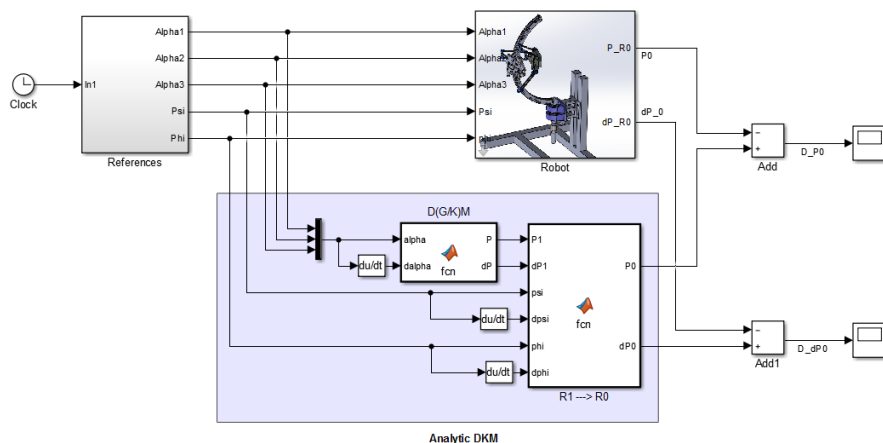


Figure 3.28: Simulink diagram

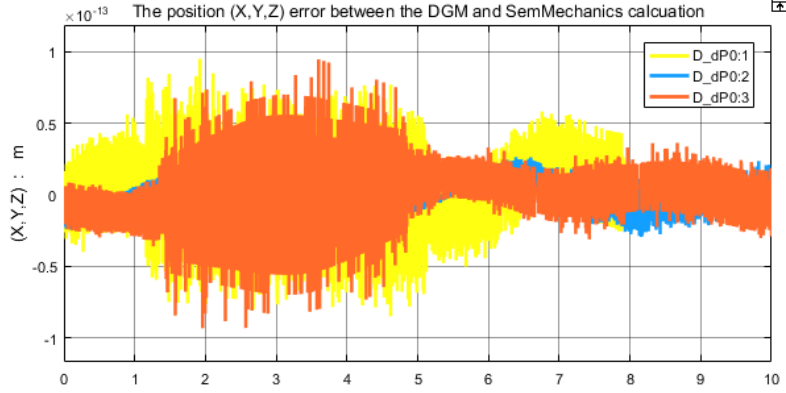


Figure 3.29: The contrast between the analytic DKM and the SimmMechanics DKM

The DKM is valid according to the simulation which shows errors around 10^{-13} .

3.4. INVERSE KINEMATIC MODEL

The objective is to know the angular velocities of the parallel structure $\frac{d\alpha_i}{dt}$ in term of the end-effector velocities $P_{/R_0}$, $\dot{\phi}$ and $\dot{\psi}$.

The IGM is described by the following function:

$$\alpha = G(X, Y, Z, \psi, \phi) = \begin{pmatrix} G_x(X, Y, Z, \psi, \phi) \\ G_y(X, Y, Z, \psi, \phi) \\ G_z(X, Y, Z, \psi, \phi) \end{pmatrix} \quad (3.60)$$

And the IKM is describes by the following equation:

$$\frac{d\alpha}{dt} = \begin{pmatrix} \frac{\partial G_x}{\partial X} & \frac{\partial G_x}{\partial Y} & \frac{\partial G_x}{\partial Z} & \frac{\partial G_x}{\partial \psi} & \frac{\partial G_x}{\partial \phi} \\ \frac{\partial G_y}{\partial X} & \frac{\partial G_y}{\partial Y} & \frac{\partial G_y}{\partial Z} & \frac{\partial G_y}{\partial \psi} & \frac{\partial G_y}{\partial \phi} \\ \frac{\partial G_z}{\partial X} & \frac{\partial G_z}{\partial Y} & \frac{\partial G_z}{\partial Z} & \frac{\partial G_z}{\partial \psi} & \frac{\partial G_z}{\partial \phi} \end{pmatrix} \cdot \begin{pmatrix} \frac{dX}{dt} \\ \frac{dY}{dt} \\ \frac{dZ}{dt} \\ \frac{d\psi}{dt} \\ \frac{d\phi}{dt} \end{pmatrix} \quad (3.61)$$

The partial derivation can be numerically calculated. However the IGM that we proposed allows to find the analitical IKM.

Given the relationship of the IGM of the delta structure, we can calculate the IKM of this mechanism:

$$\dot{\alpha} = g(P_{R_1}) \quad (3.62)$$

On the other hand we have the equation 3.19, which means:

$$\dot{P}_{R_1} = \frac{A_0''^{-1}}{dt} \cdot P_{/R_0} - A_0''^{-1} \cdot \frac{dP_{/R_0}}{dt} \quad (3.63)$$

Note that : $\frac{A_0''^{-1}}{dt} = \left(\frac{A_0''}{dt} \right)^{-1}$, this last term has been already calculated in the DKM.

It is still remaining to calculate the IKM of the delta structure $\dot{\alpha} = g(\dot{P}_{R_1})$.

The IKM of the delta structure :

We have seen in the IGM that :

$$\alpha_i = \beta_i - \delta_i \implies \dot{\alpha} = \dot{\beta}_i - \dot{\delta}_i$$

So we have to calculate $\dot{\beta}_i$ and $\dot{\delta}_i$.

1. Calculus of $\dot{\beta}_i$:

We have:

$$\tan(\beta_i) = \frac{-z_i}{x_i - r} \quad (3.64)$$

by derivation :

$$(1 + \tan(\beta_i)^2) \dot{\beta}_i = \frac{-\dot{z}_i}{x_i - r} + \frac{z_i}{(x_i - r)^2} \dot{x}_i \quad (3.65)$$

knowing the value of $\tan(\beta_i)$ (eq (3.26) page 52), this equation will be fulfilled
:

$$\dot{\beta}_i = \frac{-\dot{z}_i}{\left(1 + \frac{z_i^2}{(x_i - r)^2}\right)(x_i - r)} + \frac{z_i \dot{x}_i}{\left(1 + \frac{z_i^2}{(x_i - r)^2}\right)(x_i - r)^2} \quad (3.66)$$

Finally:

$$\dot{\beta}_i = -\frac{x_i - r}{(x_i - r)^2 + z_i^2} \dot{z}_i + \frac{z_i}{(x_i - r)^2 + z_i^2} \dot{x}_i \quad (3.67)$$

2. Calculus of $\dot{\delta}_i$:

As stated by El-Kashi's theorem :

$$e_i^2 = l_1^2 + A_i B_i^2 - 2l_1 \cdot A_i B_i \cdot \cos(\delta_i) \quad (3.68)$$

by derivation:

$$2e_i \dot{e}_i = 2 \cdot A_i B_i \cdot A_i \dot{B}_i - 2l_1 A_i \dot{B}_i \cos(\delta_i)$$

$$+ 2l_1 A_i B_i \cdot \sin(\delta_i) \dot{\delta}_i$$

It yields that :

$$\dot{\delta}_i = \frac{e_i \dot{e}_i - (A_i B_i - l_1 \cos(\delta_i)) \dot{A}_i \dot{B}_i}{l_1 A_i B_i \sin(\delta_i)} \quad (3.69)$$

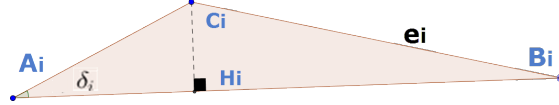


Figure 3.30: The triangle $A_i B_i C_i$

according to the figure above (figure 3.30):

$B_i H_i = A_i B_i - l_1 \cos(\delta_i)$, and the surface $l_1 A_i B_i \sin(\delta_i)$ is denoted D_i so we can write:

$$\dot{\delta}_i = \frac{e_i \dot{e}_i - B_i H_i \cdot \dot{A}_i \dot{B}_i}{D_i} \quad (3.70)$$

Calculus of $e_i \dot{e}_i$:

$$e_i^2 = l_2^2 - y_i^2 \implies e_i \dot{e}_i = -y_i \dot{y}_i \quad (3.71)$$

Calculus of $\dot{A}_i \dot{B}_i$:

$$A_i B_i^2 = z_i^2 + (x_i - r)^2 \quad (3.72)$$

$$\implies A_i B_i \cdot \dot{A}_i \dot{B}_i = z_i \dot{z}_i + (x_i - r) \dot{x}_i \quad (3.73)$$

$$\dot{A}_i \dot{B}_i = \frac{z_i \dot{z}_i}{A_i B_i} + \frac{(x_i - r)}{A_i B_i} \dot{x}_i \quad (3.74)$$

Thus:

$$\dot{\delta}_i = \frac{-y_i \dot{y}_i + \left(\frac{z_i \dot{z}_i}{A_i B_i} + \frac{(x_i - r)}{A_i B_i} \dot{x}_i \right) \cdot A_i H_i}{D_i} \quad (3.75)$$

Finally :

$$\dot{\delta}_i = \frac{A_i H_i (x_i - r)}{D_i \cdot A_i B_i} \dot{x}_i + \frac{-y_i}{D_i} \dot{y}_i + \frac{z_i \cdot A_i H_i}{D_i} \dot{z}_i \quad (3.76)$$

by doing the subtraction $\dot{\beta}_i - \dot{\delta}_i$, we find $\dot{\alpha}_i$:

$$\dot{\alpha}_i = \begin{pmatrix} \frac{z_i}{(x_i - r)^2 + z_i^2} - \frac{A_i H_i \cdot (x_i - r)}{D_i \cdot A_i B_i} \\ -\frac{y_i}{D_i} \\ \frac{-x_i - r}{(x_i - r)^2 + z_i^2} + \frac{z_i \cdot A_i H_i}{D_i} \cdot z_i \end{pmatrix}^T \begin{pmatrix} \dot{x}_i \\ \dot{y}_i \\ \dot{z}_i \end{pmatrix} \quad (3.77)$$

Also we denote:

$$G_{\alpha_i} = \begin{pmatrix} \frac{z_i}{(x_i - r)^2 + z_i^2} - \frac{A_i H_i \cdot (x_i - r)}{D_i \cdot A_i B_i} \\ -\frac{y_i}{D_i} \\ \frac{-x_i - r}{(x_i - r)^2 + z_i^2} + \frac{z_i \cdot A_i H_i}{D_i} \cdot z_i \end{pmatrix}^T \quad (3.78)$$

From $\dot{P}_i = A_i \cdot \dot{P}$, it follows that:

$$\dot{\alpha}_i = G_{\alpha_i} \cdot A_i \cdot \dot{P} \quad (3.79)$$

Finally :

$$\dot{\alpha} = \begin{pmatrix} G_{\alpha_1} \cdot A_1 \\ G_{\alpha_2} \cdot A_2 \\ G_{\alpha_3} \cdot A_3 \end{pmatrix} \dot{P} = J \cdot \dot{P} \Rightarrow J = \begin{pmatrix} G_{\alpha_1} \cdot A_1 \\ G_{\alpha_2} \cdot A_2 \\ G_{\alpha_3} \cdot A_3 \end{pmatrix} \quad (3.80)$$

3.4.1. VALIDATION

Using the model exported from SolidWorks environment to SimMechanics environment we test whether the the analytic IGM is accurate or not:

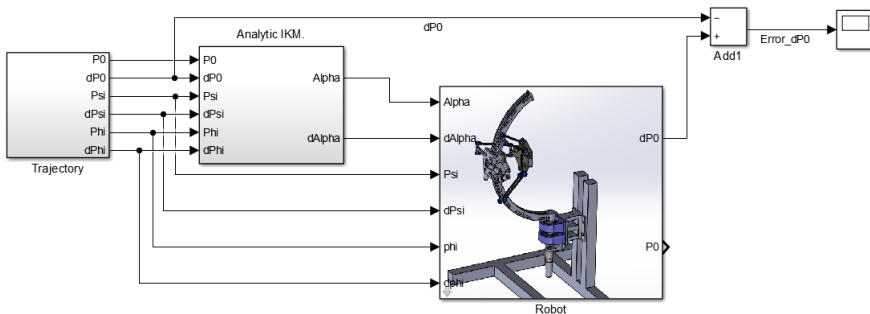


Figure 3.31: Simulink diagram to validate the DGM

The IKM will be validated implicitly as we proceeded in the IGM validation, because it is not possible to use the model imported from SolidWorks environment as an IKM.

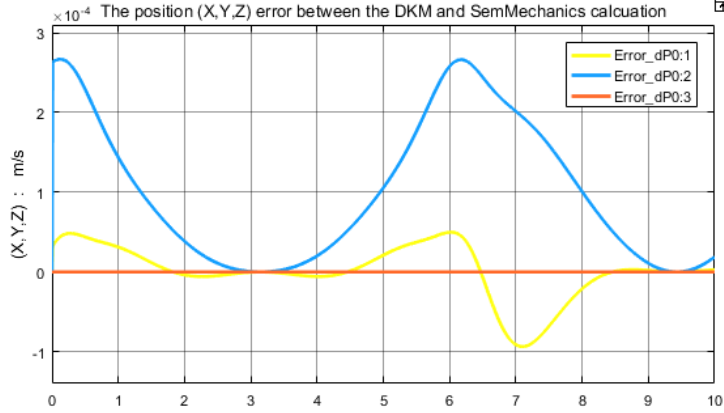


Figure 3.32: The error of the DGM

Since the order of the error between the end-effector velocity and the references is 10^{-4} , then we conclude the validity of the IKM implicitly.

3.5. THE DYNAMIC MODEL

This section presents a big importance since it is used to synthesise the control law, because it is meant to know and generate the necessary torques must be applied on each motor rotor in order that the mechanism can perform the desired task. First of all, we should note that the torque T_i given by each motor to different kinematic chains has as role to undo the gravity affects on the robot organs, and to insure that they go through the space in some specific acceleration as well:

$$T_i = T_{i_g} + T_{i_a} \quad (3.81)$$

Such that:

- T_i is the torque generated by motor i .
- T_{i_g} is the necessary torque provided by motor i to make the robot steady in front of the gravity affect, we call it the gravity torque in this report.
- T_{i_a} is the torque necessary to be provided to each actuator joints i in order that the different organs perform specific accelerations in absence of the gravity.

As it is described previously, during the operation the end effector turns around with a very low velocity. Moreover, its mass is very considerable, it is around 1 kg, which means the acceleration torque is very neglected when we come to compare it

to the gravity torque. In addition to that, the gear ratio ($n = 231$) is an important reason, as well, to ignore the acceleration torque of different robot chains, the only dynamic that will be involved is the rotor acceleration of each motor $\ddot{\theta}_i$ since it is not affected by the gearbox reduction.

That being said, the acceleration torque is reduced to $T_{ia} = J_i \ddot{\theta}_i$.

This fact allows us to have a very simplified model, rather than a very complicated one. In fact the relative dynamics of the serial and the parallel structure with respect to each other have no need to be elaborated in this work, the two robot structures can be analysed separately from each other.

The mechanical equation of each motor is :

$$T_{EL_i} = T_{ia} + T_{ig} = J_i \ddot{\theta}_i + T_{ig} \quad (3.82)$$

T_{EL_i} represents the electromagnetic torque generated by the current of the motor i .

The following study will establish the dynamic model of the delta structure, then the serial structure's.

3.5.1. THE DYNAMIC MODEL OF THE DELTA STRUCTURE

The main factor in this section is the gravity. With respect to the original base R_0 it is just a simple vector that has one component laid upon the z-axis :

$$\vec{g} = \begin{pmatrix} 0 \\ 0 \\ -9.81 \end{pmatrix} \quad (3.83)$$

Meanwhile it is a rotative vector with respect to the delta structure.

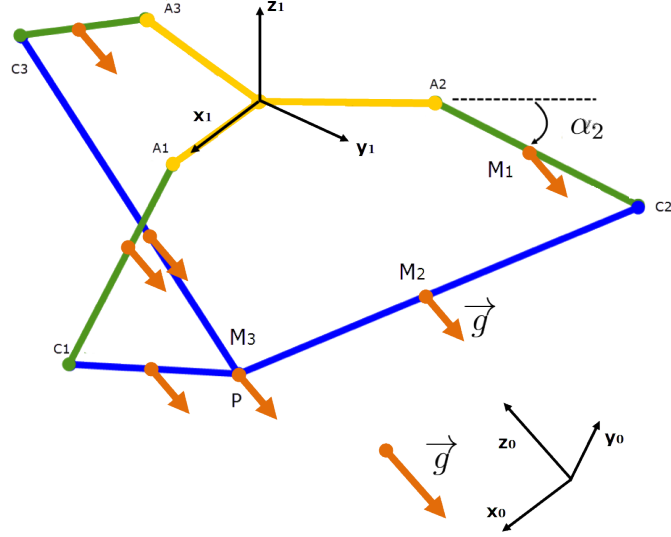


Figure 3.33: The gravity with respect to the delta structure

The gravity in the mobile base R_1 it equals to \vec{g}_1 :

$$\vec{g}_1 = A_0''^{-1} \cdot \vec{g} \quad (3.84)$$

The expression of gravity with respect to R_1 will be more compatible to calculate the gravity torque T_{1g} associated to α_1 .

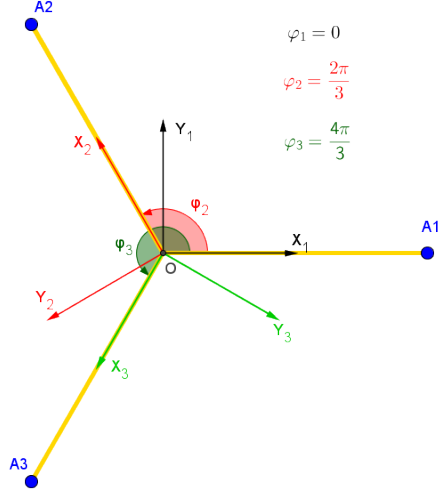


Figure 3.34: The different coordinates systems R_i associated to the slider

For the same reason we calculate the gravity with respect to the bases R_2 and R_3 so that we have the convenient expressions of the gravity in order to calculate

the gravity torques T_{2g} and T_{3g} associated respectively to α_2 and α_3 .

Let be d_1 the distance between the articulation joint A_i and the center of mass of the forearm, the center of mass of the parallel sticks is the midpoint of the segment l_2 .

Let be the following denotation :

- M_1 the mass of the forearm l_1 .
- M_2 the mass of the parallel sticks l_2 .
- M_3 the mass of the nacelle.

Having three masses M_1 , M_2 , and M_3 as illustrated in 3.33, is equivalent to having two masses M_{e1} and M_{e2} linked to the elbow C_i and the point P respectively, see the following figure.

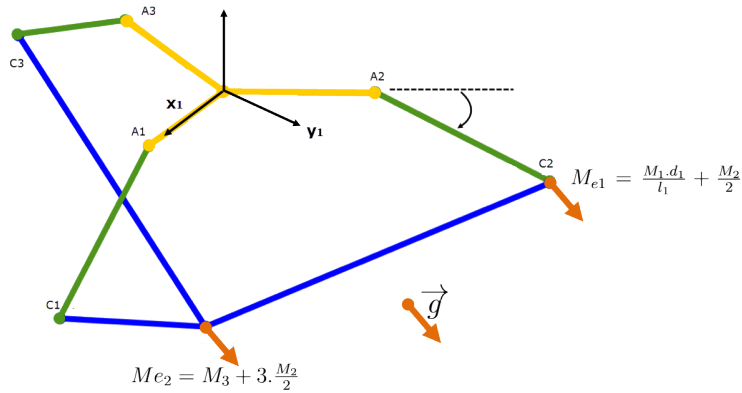


Figure 3.35: Equivalent masses

With:

$$M_{e1} = \frac{M_1 \cdot d_1}{l_1} + \frac{M_2}{2} \text{ and } M_{e2} = M_3 + 3 \cdot \frac{M_2}{2}$$

The forces due to those two masses are :

- $\vec{N}_i = \vec{g}_1 \cdot M_{e1}$ applied on the elbow C_i with $i = 1, 2, 3$
They are equal, then let them all be called \vec{N}
- $\vec{Z} = \vec{g}_1 \cdot M_{e2}$ applied at the point P

The force \vec{Z} is composed of three components carried on the parallel segments:

$$\vec{Z} = \vec{Z}_{u_1} + \vec{Z}_{u_2} + \vec{Z}_{u_3} \quad (3.85)$$

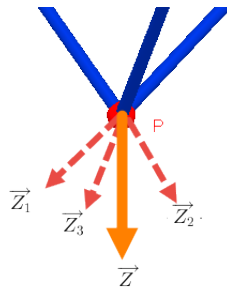


Figure 3.36: component of Z with respect to the parallel segments

Given that:

$$\begin{aligned}\vec{Z}_{u_1} &= Z_{u_1} \cdot \vec{u}_1 \\ \vec{Z}_{u_2} &= Z_{u_2} \cdot \vec{u}_2 \\ \vec{Z}_{u_3} &= Z_{u_3} \cdot \vec{u}_3\end{aligned}$$

with :

$$\vec{u}_1 = \frac{\vec{C_1P}}{C_1P}, \vec{u}_2 = \frac{\vec{C_2P}}{C_2P}, \vec{u}_3 = \frac{\vec{C_3P}}{C_3P}$$

the equation 3.85 becomes:

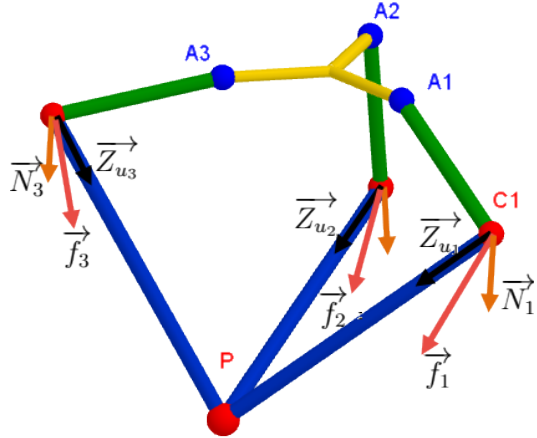
$$\vec{Z} = [\vec{u}_1 \quad \vec{u}_2 \quad \vec{u}_3] \begin{pmatrix} Z_{u_1} \\ Z_{u_2} \\ Z_{u_3} \end{pmatrix} \quad (3.86)$$

Thus the components of the force \vec{Z} with respect to the unit base $[\vec{u}_1 \quad \vec{u}_2 \quad \vec{u}_3]$ are well determined:

$$\begin{pmatrix} Z_{u_1} \\ Z_{u_2} \\ Z_{u_3} \end{pmatrix} = [\vec{u}_1 \quad \vec{u}_2 \quad \vec{u}_3]^{-1} \vec{Z} \quad (3.87)$$

The total force applied on each elbow C_i is :

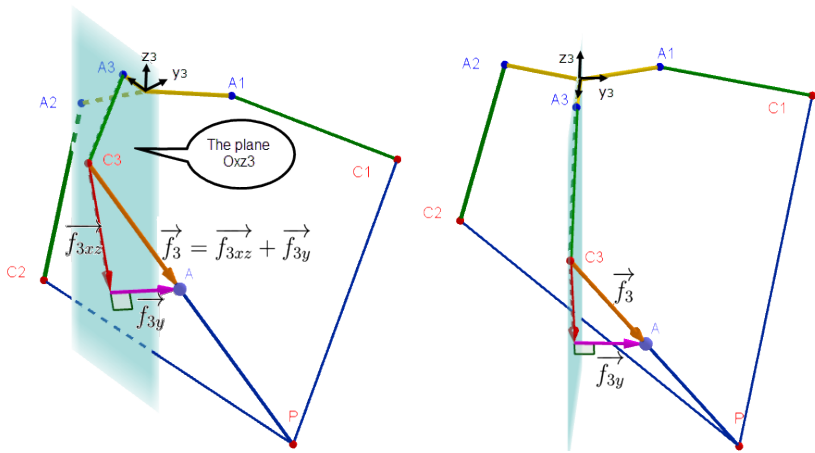
$$\vec{f}_i = \vec{Z}_{u_i} + \vec{N}$$


 Figure 3.37: The forces applied on each elbow C_i

Each elbow i belongs to its associated base R_i , so having the force \vec{f}_i expressed in this base will be more convenient to next calculations. To have that, we multiply \vec{f}_i by $A_i^{-1} = A_i^T$, this matrix is elaborated in 3.1.

More over, each forearm has its freedom only in the plane Oxz_i , which means the only component of \vec{f}_i that has mechanical work is f_{ixz} , the component f_{iy} has no effect 3.38.

$$\vec{f}_{ixz} = \underbrace{\begin{pmatrix} 1 & 0 & 0 \\ 0 & 0 & 0 \\ 0 & 0 & 1 \end{pmatrix} \cdot A_i^T \vec{f}_i}_{\text{let it be denoted } B}$$


 Figure 3.38: The projection of the force f_3 on the plane Oxz_3

Finally The torque due to the gravity applied on each forearm i with respect to its joint is :

$$(0 \quad 1 \quad 0) \cdot (\overrightarrow{AC_i} \times \overrightarrow{f_{ixz}}) \quad (3.88)$$

Finally:

$$T_{ig} = - (0 \quad 1 \quad 0) \cdot (\overrightarrow{AC_i} \times \overrightarrow{f_{ixz}}) \cdot \frac{1}{231} \quad (3.89)$$

The dot product has appeared because the torque vector calculated in 3.88 has no component on the plane Oxz_i , but only one component on y-axis which has effect on the forearm.

The minus sign has been introduced because the torque provided to the joint i must oppose the gravity torque in order to prevent its effect on the elbow.

The number 231 represents the gearbox ratio, so dividing by this ratio, we get the torque must be generated by the motor i .

3.5.2. THE DYNAMIC MODEL OF THE SERIAL STRUCTURE

The gravity has no effect on the fifth joint (ϕ), then $T_{5g} = 0$.

Whereas the gravity effects the fourth actuator, associated to (ψ), substantially by the end-effector mass M_3 and the slider mass M_4 as it is illustrated in the figure below:

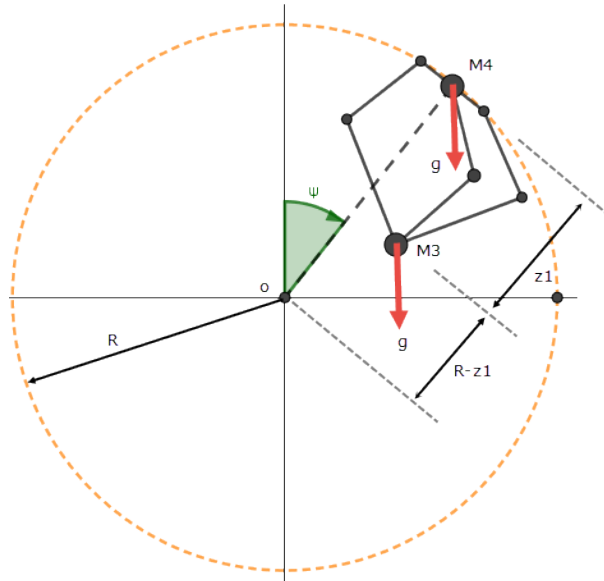


Figure 3.39: The substantial forces that generate T_{4g}

The torque generated with respect to the point O is :

$$C = ((R - z_1) \cdot M_3 + R \cdot M_4) \cdot \sin(\psi) \quad (3.90)$$

The torque due to the masses of the kinematic chains can be introduced in the previous equation, approximately as following:

$$C = \left((R - z_1) \cdot \left(M_3 + 3 \cdot \frac{M_1 + M_2}{2} \right) + R \cdot \left(M_4 + 3 \cdot \frac{M_1 + M_2}{2} \right) \right) \cdot \sin(\psi) \quad (3.91)$$

The power provided by the pulley is the same as an actuator generating a torque C , hypothetically placed at the center O .

Let C' be the torque generated by the pulley, then :

$$C' \cdot d\psi' = C \cdot d\psi$$

ψ' is the rotation angle of the pulley. Since there is no sliding between it and the arc as it is demonstrated in the figure 3.40, then:

$$d\psi = d\psi' \cdot \frac{R_p}{R}$$

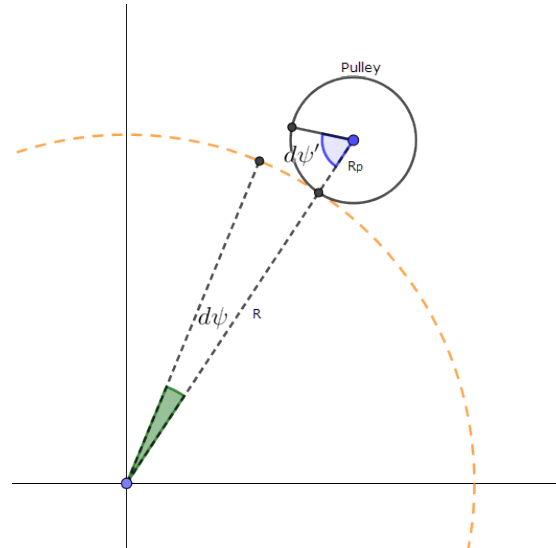


Figure 3.40: The relation between the pulley rotation and ψ

Thus :

$$C' = C \cdot \frac{R_p}{R}$$

Finally, the torque provided by the motor 4 linked to the pulley is :

$$T_{4g} = \frac{C'}{231}$$

It yields that:

$$\boxed{T_{4g} = \left((R - z_1) \cdot \left(M_3 + 3 \cdot \frac{M_1 + M_2}{2} \right) + R \cdot \left(M_4 + 3 \cdot \frac{M_1 + M_2}{2} \right) \right) \cdot \sin(\psi) \frac{R_p}{231.R}} \quad (3.92)$$

Note that the rotor rotation angel of the motor 4 is :

$$\theta_4 = \frac{231.R}{R_p} \psi$$

The dynamic modeling is accomplished.

3.5.3. VALIDATION

The model calculated is compared in this paragraph to the numeric model imported from SolidWorks environment. During the simulation the mass was real, whereas the velocity was not low as it was described previously, it was considerable to know the extent of model accuracy.

the diagram of simulation:

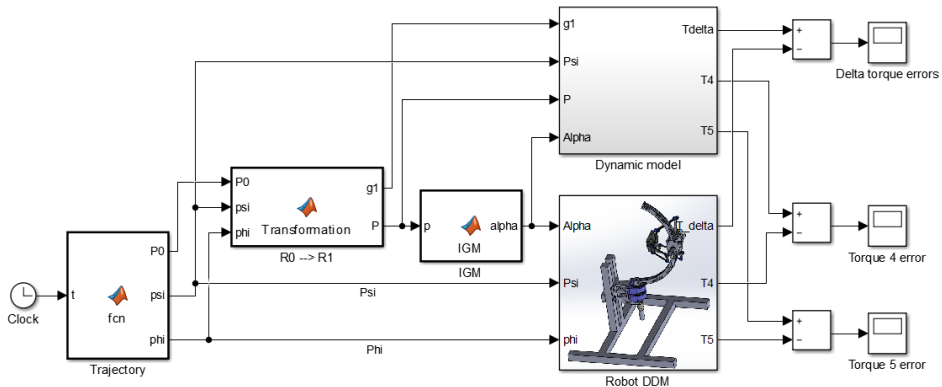


Figure 3.41: Simulink diagram to test the dynamic model

The comparison shows the following differences :

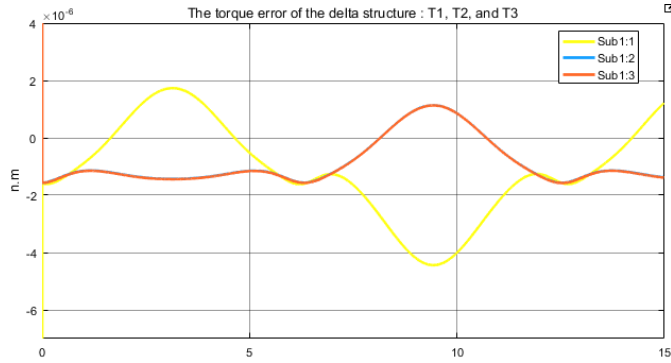


Figure 3.42: Torque error signal of the delta structure

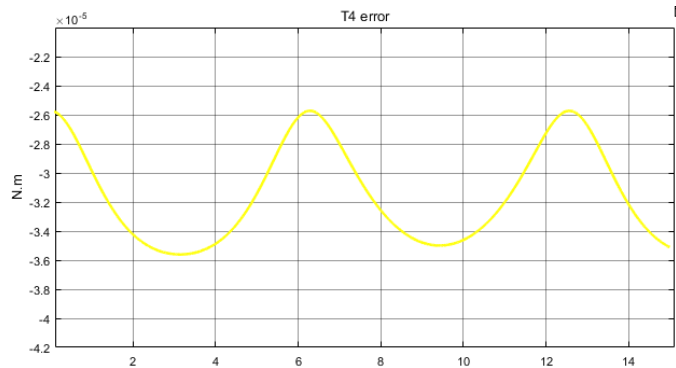


Figure 3.43: Torque error signal of the fourth actuator

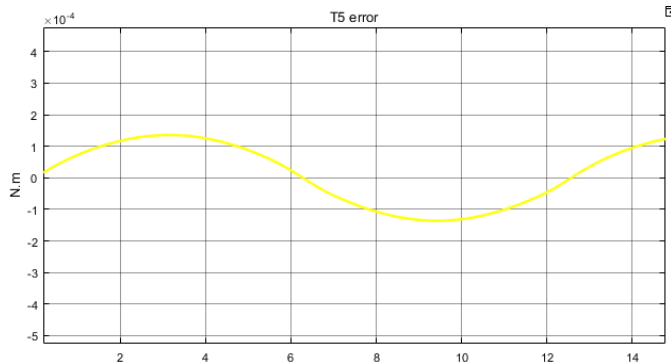


Figure 3.44: Torque error signal of the fifth actuator

Even though the movement of the robot was fast, the first reason to not calculate the dynamics of the different organs is still fulfilled here. In fact the simulation

CHAPTER 3. MODELLING

shows the models are well accurate since the errors are 10^{-6} , 10^{-5} , 10^{-4} , the extent of this accuracy despite of the taken velocity was out of expectation!

Chapter 4

Control

Contents

4.1	The state model	76
4.2	The control strategy	78
4.3	The electrical subsystem control	79
4.4	The mechanical subsystem control	81
4.5	Validation (SimMechanics)	89
4.6	Experimentation	92

4.1. THE STATE MODEL

In this system, the state variables are: the rotation angels ($\theta_1, \theta_2, \theta_3, \theta_4$, and θ_5), their angular velocities, and the current of each motor. The tensions u_1, u_2, u_3, u_4 and u_5 are the system inputs.

According to the electrical relationships of DC motors, we write for each motor

$$u_i = R \cdot I_i + L \cdot \frac{dI_i}{dt} + K \cdot \frac{d\theta_i}{dt} \quad (4.1)$$

With:

R represents the electrical resistance.

L represents the induction.

K is the velocity constant (it equals to the torque constant).

The previous equation can written as:

$$\dot{I}_i = -\frac{R}{L} \cdot I_i - \frac{K}{L} \cdot \dot{\theta}_i + \frac{1}{L} u_i \quad (4.2)$$

Let us recall the mechanical equation of each motor (3.82):

$$\ddot{\theta}_i = \frac{1}{J} \cdot T_i - \frac{1}{J} \cdot T_{ig} \quad (4.3)$$

The relation between the electrical equation and the mechanical equation is the electromagnetic torque:

$$T_i = K \cdot I_i \quad (4.4)$$

Let be the following denotations:

$$a_3 = \frac{K}{J}, \quad a_g = \frac{-1}{J}, \quad b_1 = \frac{1}{L}, \quad b_2 = \frac{-K}{L}, \quad \text{and} \quad b_3 = \frac{-R}{L}.$$

and :

$$x_1 = \theta_i, \quad x_2 = \dot{\theta}_i, \quad \text{and} \quad x_3 = I_i$$

Then, each motor state model will be as following:

$$\begin{cases} \dot{x}_1 = x_2 \\ \dot{x}_2 = a_3 \cdot x_3 + a_g \cdot T_{ig} \\ \dot{x}_3 = b_3 \cdot x_3 + b_2 \cdot x_2 + b_1 \cdot u_i \end{cases} \quad (4.5)$$

The whole robotic system model is then illustrated as :

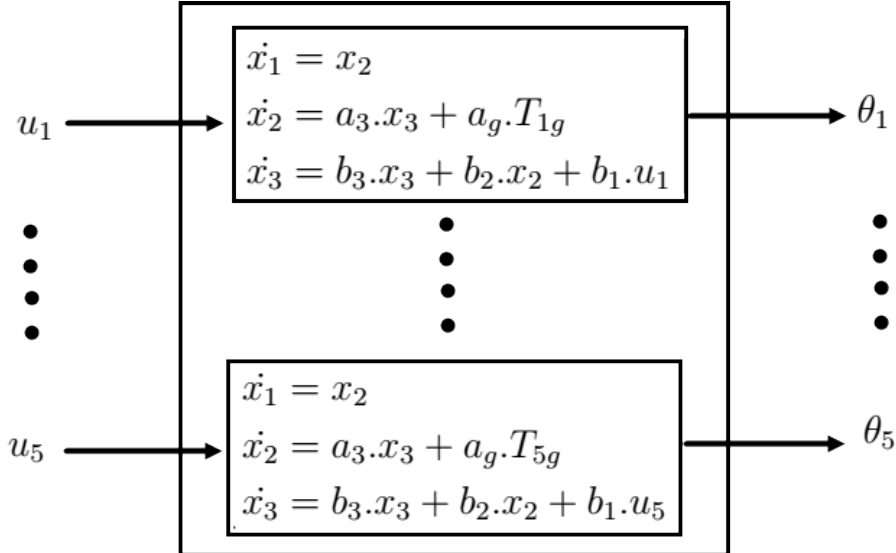


Figure 4.1: State model diagram

This is a coupled non-linear system of 15 state variables.

4.2. THE CONTROL STRATEGY

Things to be noticed in the state model 4.14 before starting tuning the control law. The state model includes two subsystems: the electrical subsystem and the mechanical subsystem, the first one which is a linear, has the tension u_i as its input and provides its output x_3 to the mechanical subsystem. The non-linearity of this state model lies within the torque T_{ig} , which, moreover, effects interactions between the whole system different motors (the whole robotic system is coupled). In fact, $T_{ig}(\theta_1, \theta_3, \theta_4, \theta_5)$ is a function of the five rotation angels. Further more, if we have taken in account the acceleration torque in the modelling chapter, the interaction and the non-linearity will be a function of currents and angular velocities in addition to the angels themselves.

Consequently, the state model of each motor can be illustrated as:

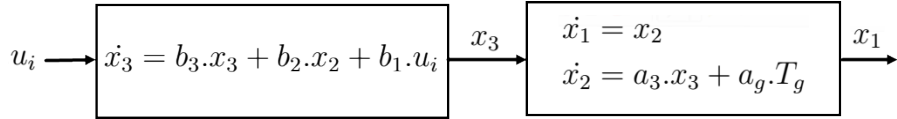
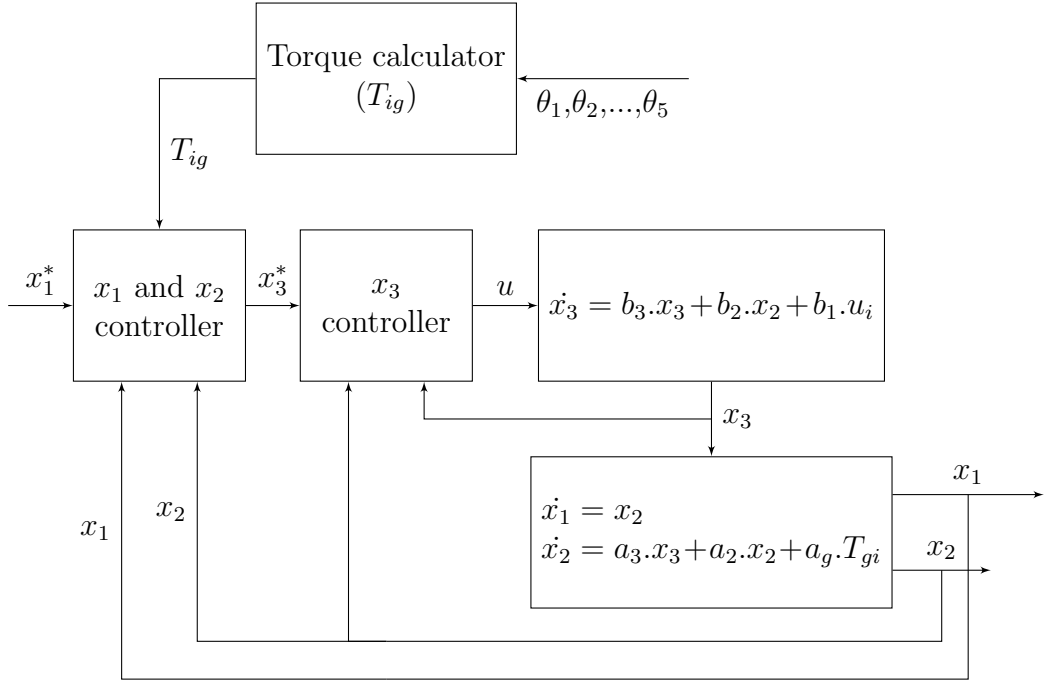


Figure 4.2: State model diagram

The state model diagram as represented is useful to apply a straightforward control law. For instance, it brings to mind the idea to control the mechanical subsystem output (the angel) via its inputs (current), which itself is the electrical subsystem output. Once the current desired to control the angel is calculated, we control the electrical system output (the current) via its input (tension) to realize this desired current. Thus, it is a cascade of two controllers:



4.3. THE ELECTRICAL SUBSYSTEM CONTROL

The electrical equation :

$$\begin{cases} \dot{x}_3 = b_3.x_3 + b_2.x_2 + b_1.u_i \end{cases} \quad (4.6)$$

This subsystem is interacted with the mechanical subsystem by the effect of the velocity. Applying the following simple decoupling state feedback $u_i = \frac{-b_2.x_2 + v_i}{b_1}$ will undo that interaction. The equivalent system yielded is :

$$\begin{cases} \dot{x}_3 = b_3.x_3 + v_i \end{cases} \quad (4.7)$$

It is a first order system, its frequency representation is.

$$G(s) = \frac{1}{s - b_3} \quad (4.8)$$

The objective is not to stabilize the process (the eigenvalue is already negative), but to enhance its performance/robustness and its servo/regulation. A simple PI controller will be sufficient for that :

$$R(s) = C_p + \frac{C_I}{s} = C_p \frac{s + \frac{C_I}{C_p}}{s} \quad (4.9)$$

The open loop:

$$R(s).G(s) = C_p \frac{s + \frac{C_I}{C_p}}{s} \cdot \frac{1}{s - b_3} \quad (4.10)$$

Let $\frac{C_I}{C_p}$ equal to $-b_3$, then :

$$R(s).G(s) = \frac{C_p}{s} \quad (4.11)$$

The closed loop will be:

$$T = \frac{R(s).G(s)}{1 + R(s).G(s)} = \frac{C_p}{C_p + s} \quad (4.12)$$

Let $-2.b_3$ be the desired eigenvalue, then

$$\begin{cases} C_p = -2.b_3 \\ C_I = -2.b_3^2 \end{cases} \quad (4.13)$$

Analysis

The closed loop system (the complementary sensitivity function) is first order system, that means:

- The process response is very fast, and has no oscillation as well (performance).
- The robustness is ensured, we can conclude that directly from the Nyquist diagram:

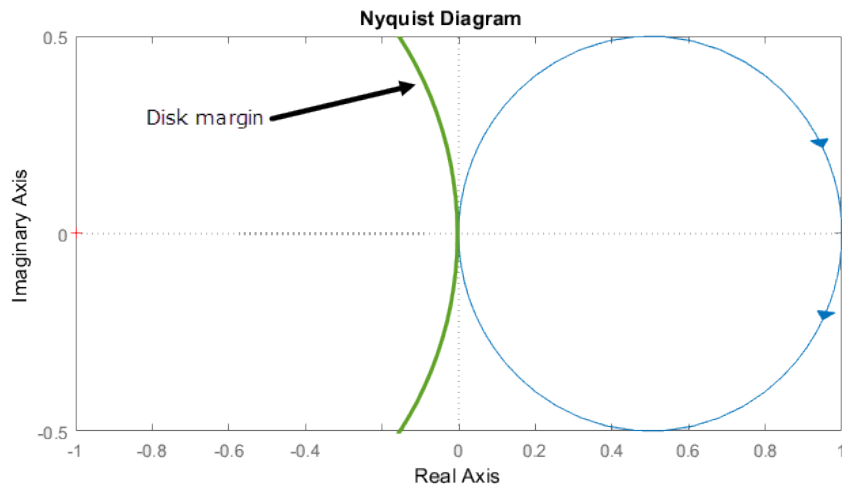


Figure 4.3: Nyquist diagram of T

It is clear that the module margin (the inverse of the sensitivity function $|S(s)|$) is no lesser than one.

- The Bode diagram of T shows us the controller effectiveness in term of regulation:

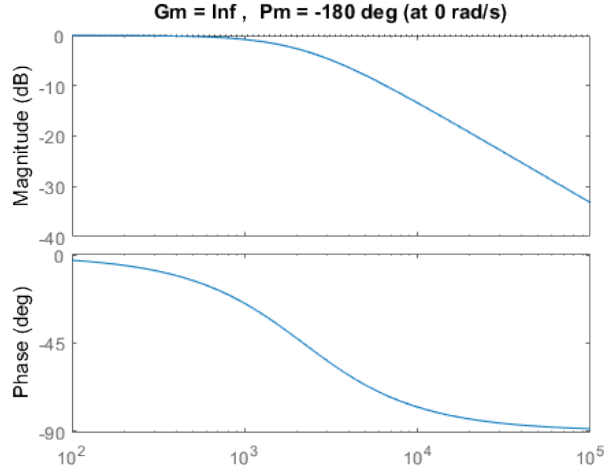


Figure 4.4: Bode diagram of T

At low frequency, we notice that $T = 1$ (or $S = 0$), which means that tracking error will be null, and the input errors are rejected. Also, at high frequency: $T = 0$ (or $S = 1$), which implies that the measure noises are rejected as well.

4.4. THE MECHANICAL SUBSYSTEM CONTROL

The mechanical subsystem is represented by the following equations:

$$\begin{cases} \dot{x}_1 = x_2 \\ \dot{x}_2 = a_3.x_3 + a_g.T_{ig} \end{cases} \quad (4.14)$$

Let consider the following feedback: $x_3 = \frac{-a_g.T_g + V}{a_3}$, the point is to linearise and decouple the system and get this simple process:

$$\begin{pmatrix} \frac{dx_1}{dt} \\ \frac{dx_2}{dt} \end{pmatrix} = \begin{pmatrix} 0 & 1 \\ 0 & 0 \end{pmatrix} \cdot \begin{pmatrix} x_1 \\ x_2 \end{pmatrix} + \begin{pmatrix} 0 \\ 1 \end{pmatrix} \cdot v \quad (4.15)$$

Where : v is the new equivalent input.

This system ($G(s) = \frac{1}{s^2}$) has two unstable eigenvalues, The objective then, is to

design a controller $R(s)$ as to stabilize $G(s)$ and meet the following specifications as well, we seek to:

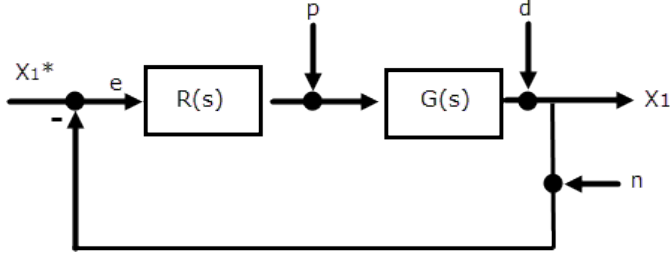


Figure 4.5: The control scheme

- Reduce by at least $-60db$ of the influence of the input and output perturbations: p and d , in the frequency domain $w \in [0, w_d]$, with $0.1 \leq w_d \leq 1$.
- Follow with error less than or equal to $-40db$ the reference signal x_1^* within the frequency band : $[0, w_r]$, where $w_r \geq$
- Attenuate by at least $-50db$ in the frequency band $[10^3, \infty[$.
- Statistic error in response to sinusoidal reference must be zero.
- The time response must be at most 0.2 seconds
- The stability margins must be taken in account.

The first three items brings conditions on the sensitivity function $S(s)$ and its complementary $T(s)$:

$$\begin{cases} |S(s)| \leq -80db & , \quad w \in [0, w_d] \\ |S(s)| \leq -40db & , \quad w \in [0, w_r] \\ |T(s)| \leq -50db & , \quad w \in [w_n, \infty[\end{cases} \quad (4.16)$$

Such as:

$$S(s) = \frac{1}{1+R(s).G(s)} \text{ and } T(s) = \frac{R(s).G(s)}{1+R(s).G(s)}, \text{ with } L(s) = R(s).G(s).$$

Thus, it will be sufficient to realize the following inequalities in order to ensure the desired conditions:

$$\begin{cases} |L(s)| \geq 80db & , \quad w \in [0, w_d] \\ |L(s)| \geq 40db & , \quad w \in [0, w_r] \\ |L(s)| \leq -50db & , \quad w \in [w_n, \infty[\end{cases} \quad (4.17)$$

The process and the conditions boundaries are illustrated below:

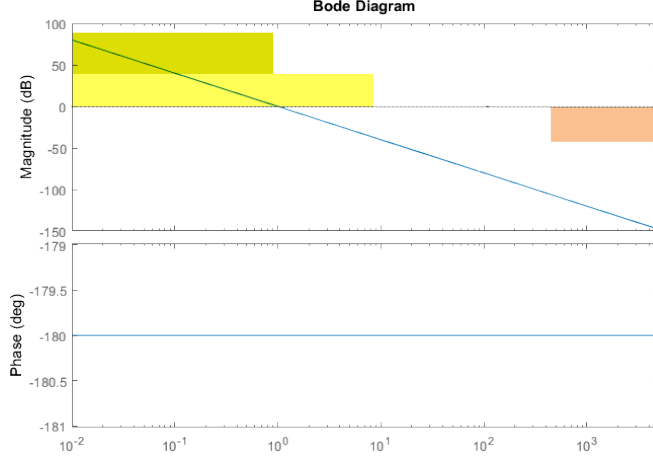


Figure 4.6: The process with respect to the loop shaping boundaries

The fourth condition is ensured, in fact:

$$\lim_{t \rightarrow \infty} e(t) = \lim_{s \rightarrow 0} s.E(s) = \lim_{s \rightarrow 0} s \cdot \frac{w}{s^2 + w^2} \cdot \frac{1}{1 + R(s)/s^2} = 0 \quad (4.18)$$

Moreover, Even the response error to a parabolic reference (t^2) can less then 0.02:

$$\lim_{t \rightarrow \infty} e(t) = \lim_{s \rightarrow 0} s.E(s) = \lim_{s \rightarrow 0} s \cdot \frac{2}{s^3} \cdot \frac{1}{1 + R(s)/s^2} = \frac{2}{R(0)} \quad (4.19)$$

If $R(0) > 100$ then the error will be less then 0.02.

The simple controller, that might go through mind at first, is a simple gain $R(s) = 1000$, Multiplying the process by 1000 will verify surely all conditions except the last ones.

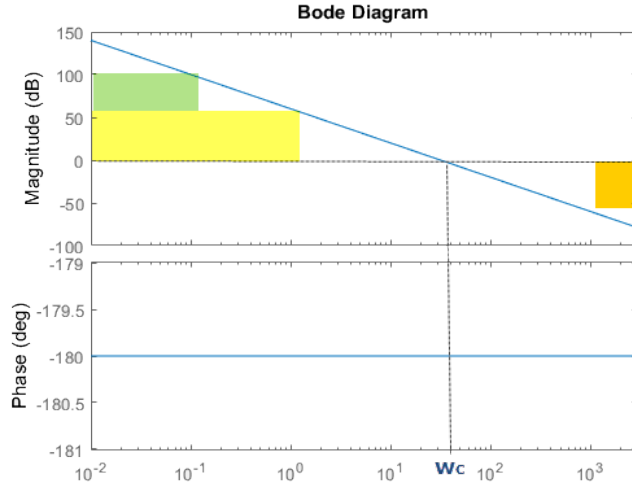


Figure 4.7: The process with respect to the loop shaping boundaries

The constraints are well met and respected. But, the stability margins must be enhanced here.

The phase margin is 0° . Meanwhile the robustness phase margin must be no lesser than 45° .

A suitable solution for that is to introduce a phase lead compensator, The usual one has this typical form: [4]:

$$\frac{Kc.(1+T.s)}{1+\alpha.T.s}$$

Its Bode diagram:

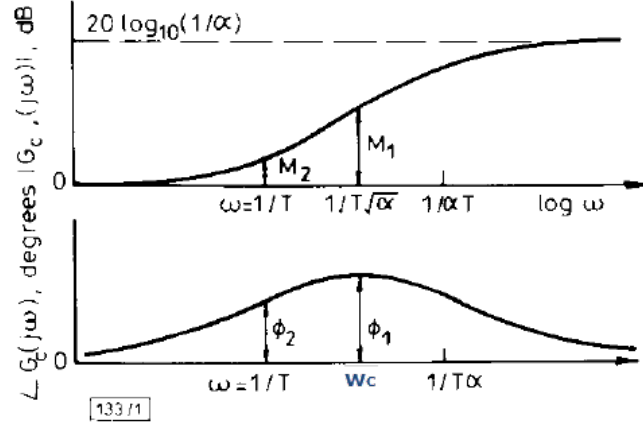


Figure 4.8: Frequency plots for phase load compensator[4]

However, introducing such compensators is not systematic and may alter the shaped process ($1000.G$), For instance, the maximum of this corrector is not zero

(in db) (see the previous figure), which brings the problem that when the designer introduces the compensator to correct the margin phase at the point w_c , the cut-off frequency w_c changes as well. Consequently, the margin phase itself changes again. So the designer needs, each time, to verify and correct the phase margin and the cut-off frequency again.

In this light, we worked to design this new compensator below, which is very systematic, and for which we need just to know the cut-off frequency w_c and the additional phase ϕ_{max} in order to tune it:

$$C(s) = \beta \cdot r - r \cdot \frac{1 - \alpha \cdot s}{1 + \alpha \cdot s} \quad (4.20)$$

With:

$$\begin{cases} \alpha = \frac{\tan(\frac{\pi}{4} - \frac{\phi_{max}}{2})}{w_c} \\ \beta = \frac{1}{\sin(\phi_{max})} \\ r = \frac{1}{\sqrt{\beta^2 - 1}} \end{cases} \quad (4.21)$$

Having $w_c = 31.6$ rad/sec, and different values for $\phi_{max} \in \{45^\circ, \dots, 85^\circ\}$, The Bode plots look like:

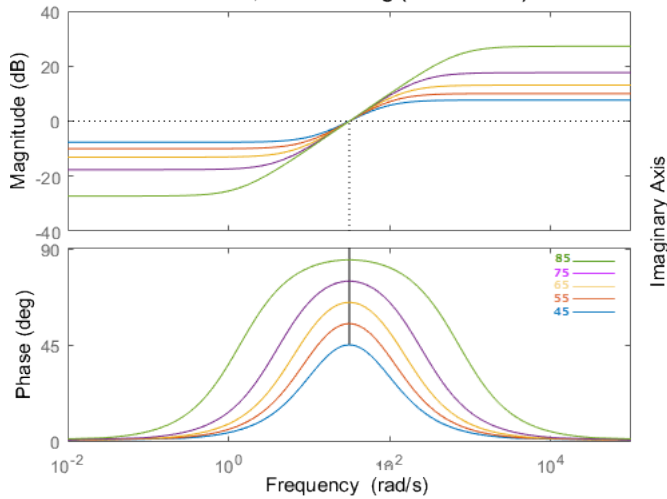


Figure 4.9: Frequency plots for phase load compensator

As expected and wanted, we got the corrector magnitude null at the cut-off frequency: $|C(w_c)| = 0$, together with: $\angle C(w_c) = \phi_{max}$. However, the more ϕ_{max} is increased (in order to enhance the robustness as illustrated in the figure(a) below), the more the magnitude curve is far away from zero-axis at low and high frequencies which makes the open loop magnitude curve closer to the frequencies

axis.

That being said, and knowing that increasing ϕ_{max} is mandatory for robust stability, as well as getting the open loop system magnitude curve far away from the zero-axis is vital for regulation issues (rejection of the disturbances), Then we can say that ϕ_{max} is a parameter of overlap between the desired regulation specifications and the desired robustness. Hence a trade-off between robustness and regulation must be done.

According to the sensitivity functions plots(figure (b) below) and the the compensators Bode diagrams in the figure above, the range [65 75] includes the best values of ϕ_{max} for which the desired module margin is fulfilled (see $\sup |S(s)|$ for each ϕ_{max} , in the figure above), and the compensator magnitude is reduced as well (see the figure (b) below).

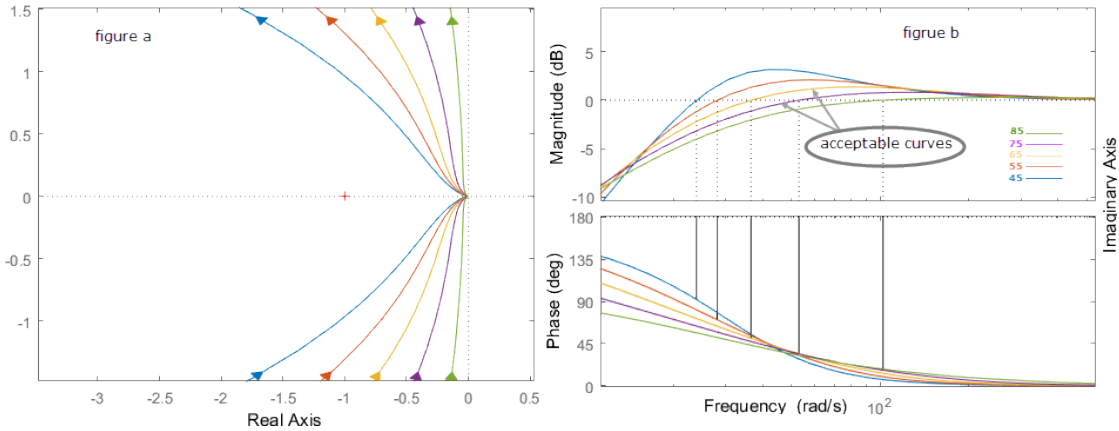


Figure 4.10: Figure (a): The Nyquist diagram for the open loop system $L(s)$. Figure (b): The frequency plots for the sensitivity functions $S(s)$.

Taking $\phi_{max} = 75^\circ$, we get this open loop system Bode diagram:

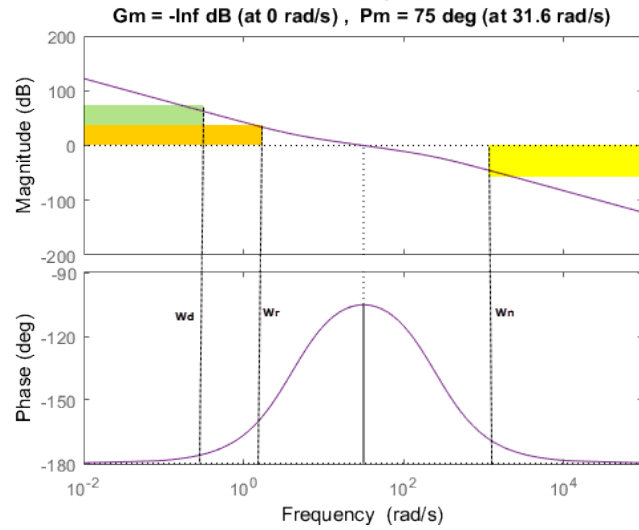


Figure 4.11: Frequency plots for the open loop system

We can notice now, that all specifications mentioned previously, are well met. And surprisingly, the gain margin is ∞ , and the module margin is well tuned (the curve is far away from -1) which means that $\sup(|S(s)|)$ is well optimized.

The last thing to be checked here is whether the curve encounters -1 or not as the variable s goes closer and closer to 0. Excluding the two null eigenvalues from the Nyquist contour on the right plan covered by $L(s)$, the complete diagram of $L(s)$ will be:

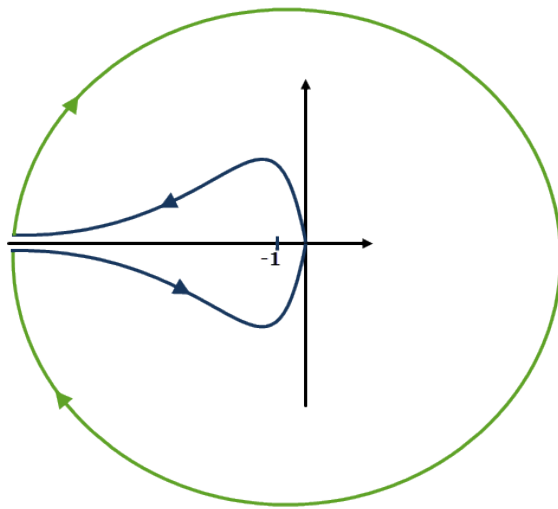


Figure 4.12: Nyquist theorem

There is no positive eigenvalue inside the Nyquist contour ($P = 0$), and there is no encirclement around -1 ($N = 0$). Therefore, no positive pole is expected to be in the closed loop system ($Z = 0$).

The simulation of this controller:

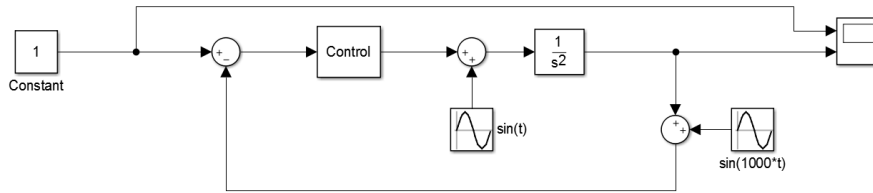


Figure 4.13: Simulink diagram for loop shaping control

The controller has been tested with a unit reference, an input perturbation ($\sin(t)$), and measurement noise ($\sin(1000t)$), the result is:

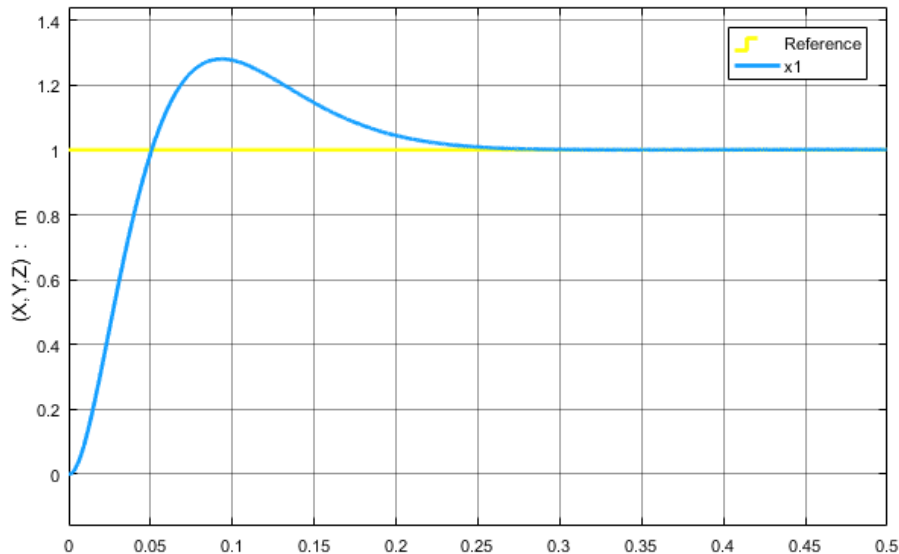


Figure 4.14: Simulation of loop shaping controller

The noises and perturbations are well rejected. Additionally, there is no tracking error. That shows that the controller is well tuned and verifies all the desired specifications.

4.5. VALIDATION (SIMMECHANICS)

This validation aims to use the model exported from SolidWorks environment to SimMechanics environment to test the control strategy on the whole system:

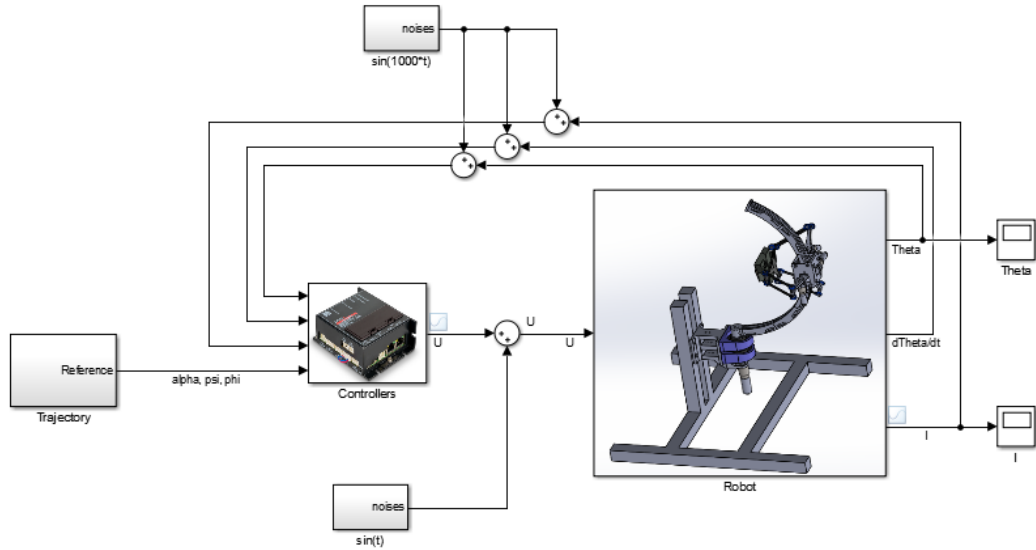


Figure 4.15: The Simulink diagram for the whole closed loop system

The Block ,called trajectory, provides to the controller the necessary actuators signals ($\alpha_1, \alpha_2, \alpha_3, \psi$, and ϕ) calculated using an IGM introduced inside of it. All the signal wires are vectors of 5 variables, for example:

$$U = \begin{pmatrix} u_1 \\ u_2 \\ u_3 \\ u_4 \\ u_5 \end{pmatrix}, \quad \text{Theta} = \begin{pmatrix} \theta_1 \\ \theta_2 \\ \theta_3 \\ \theta_4 \\ \theta_5 \end{pmatrix}$$

Input perturbations at low frequency ($w = 1$), and measurement noises at high frequency ($w = 1000$), are introduced as

The test gives this following results:

CHAPTER 4. CONTROL

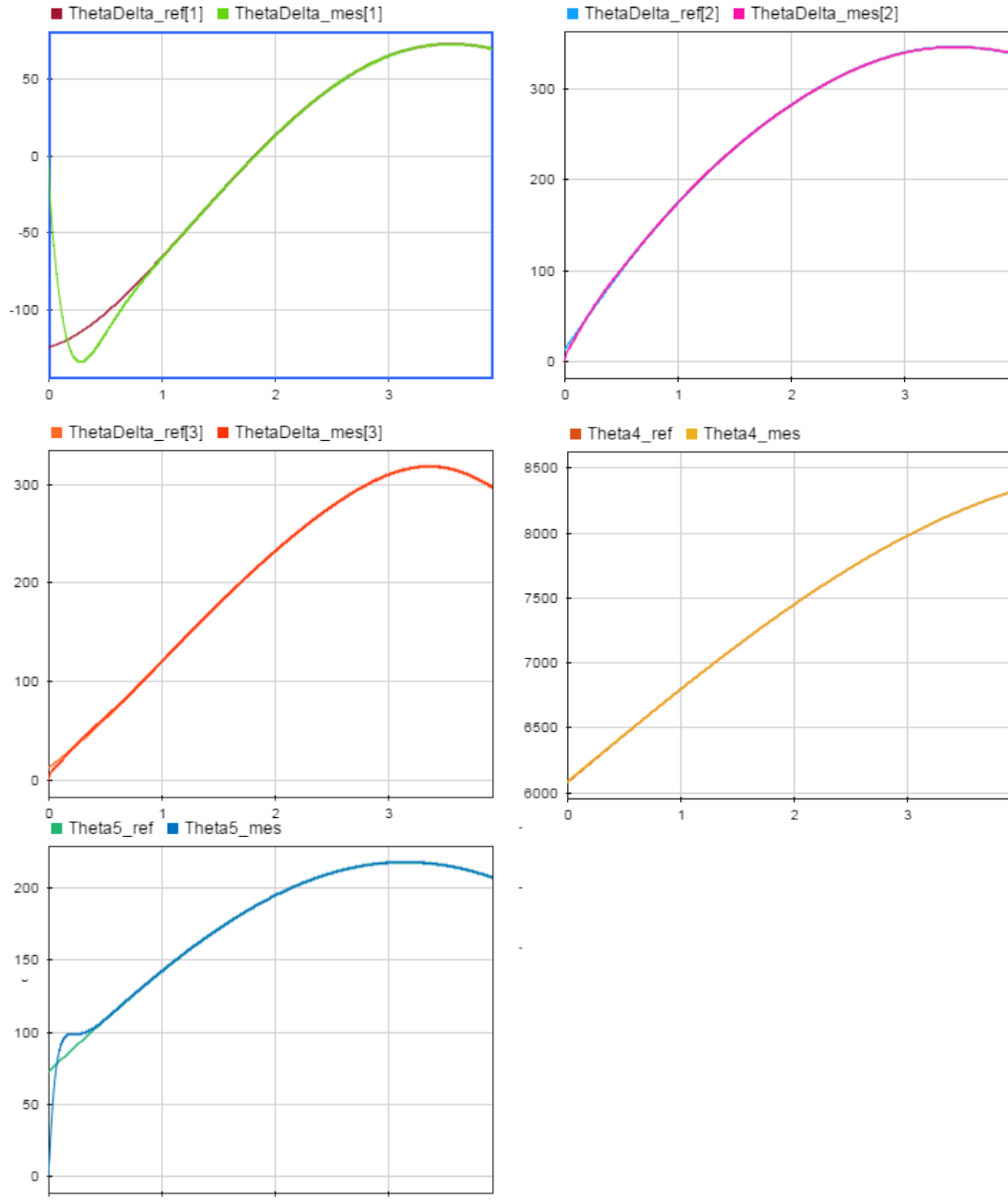


Figure 4.16: Comparison between the references and the measurements of the angles

Despite the disturbances presence, the outputs still track with no static error the references. That proves the controller performances together with its regulations capacities, and implicitly its robustness as well.

The current margin is 2A for all motors, except the fifth one for which the

CHAPTER 4. CONTROL

current must not exceed 5A, those margins are well respected:

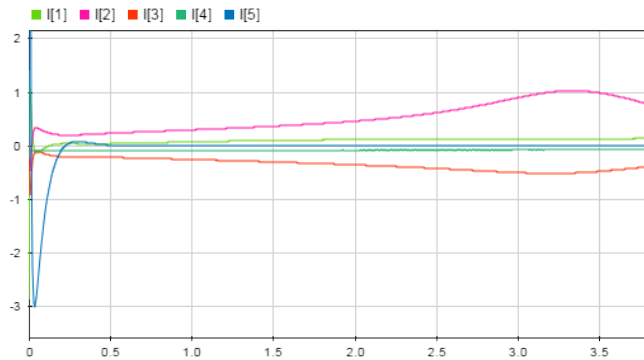


Figure 4.17: The current measurements (1 unit = 1 A)

4.6. EXPERIMENTATION

Finally, After printing the different mechanism organs, they were jointed together to make a prototype controlled via a computer using LabVIEW software and Maxon controllers. this phase of work needs in fact a whole chapter to cover and discuss all what has been done like how the electrical wiring has been done between the motors, the controllers, and the computer. and how we programme the computer using Labview. Nevertheless, for time reason we will proceed to show the general picture of this phase work, without talking about details.

The prototype:

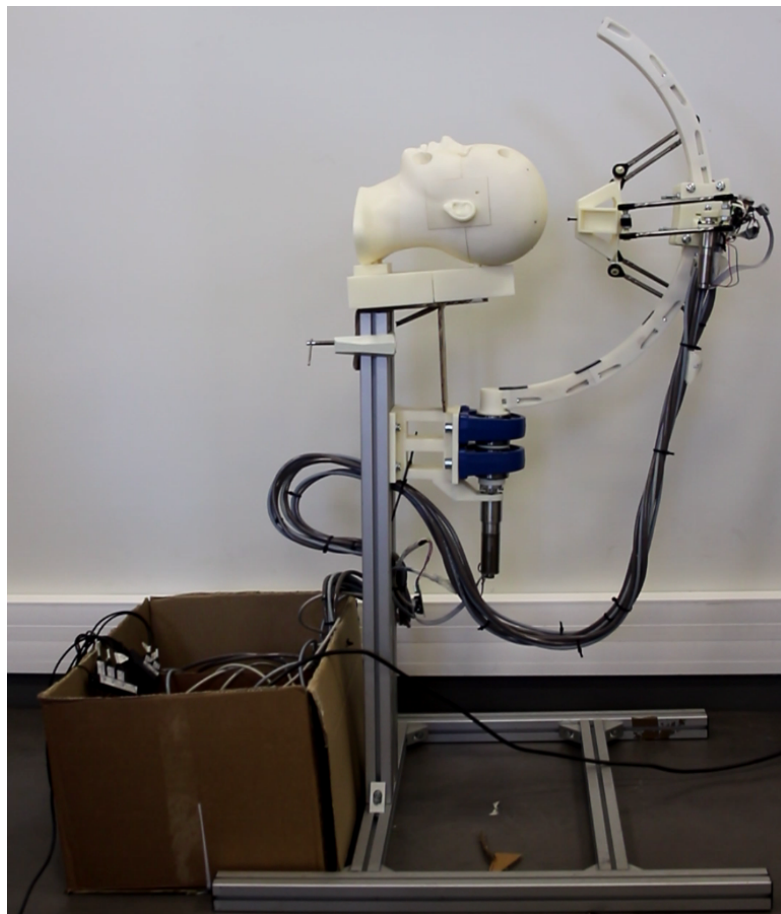


Figure 4.18: The prototype

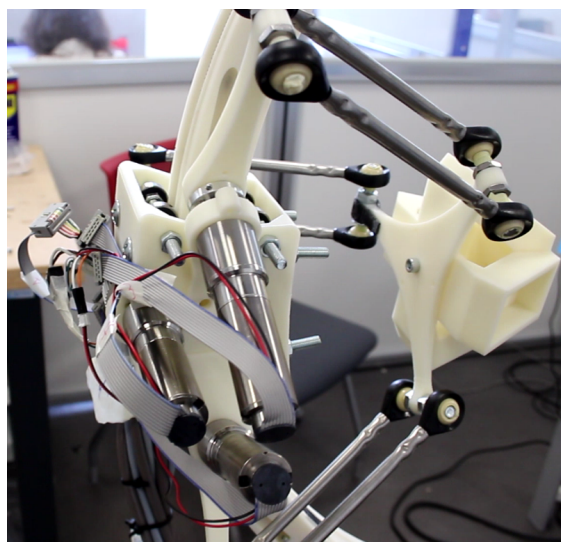


Figure 4.19: The prototype

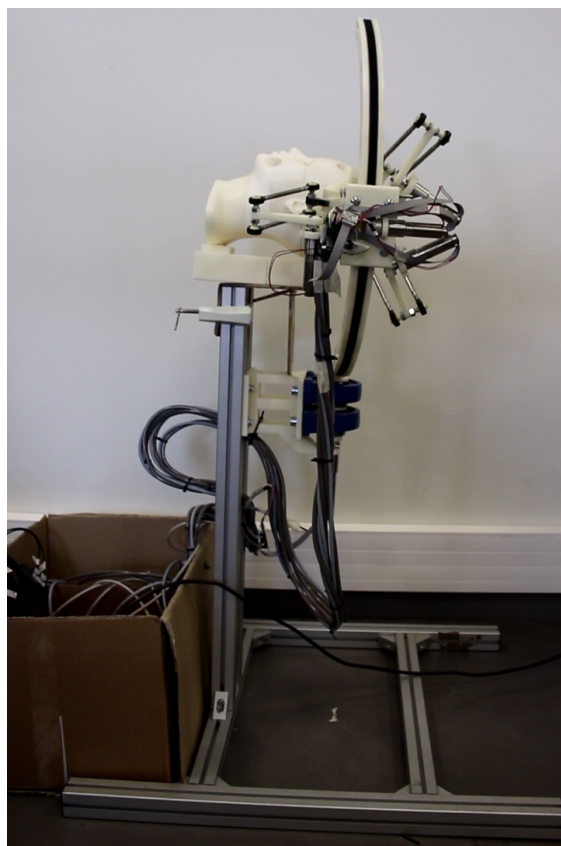


Figure 4.20: The prototype

CHAPTER 4. CONTROL

The Maxon controller are programmed with PID (it is not possible to change the control law implemented inside of it).

The experimentation shows that the outputs (angels) follow their references.

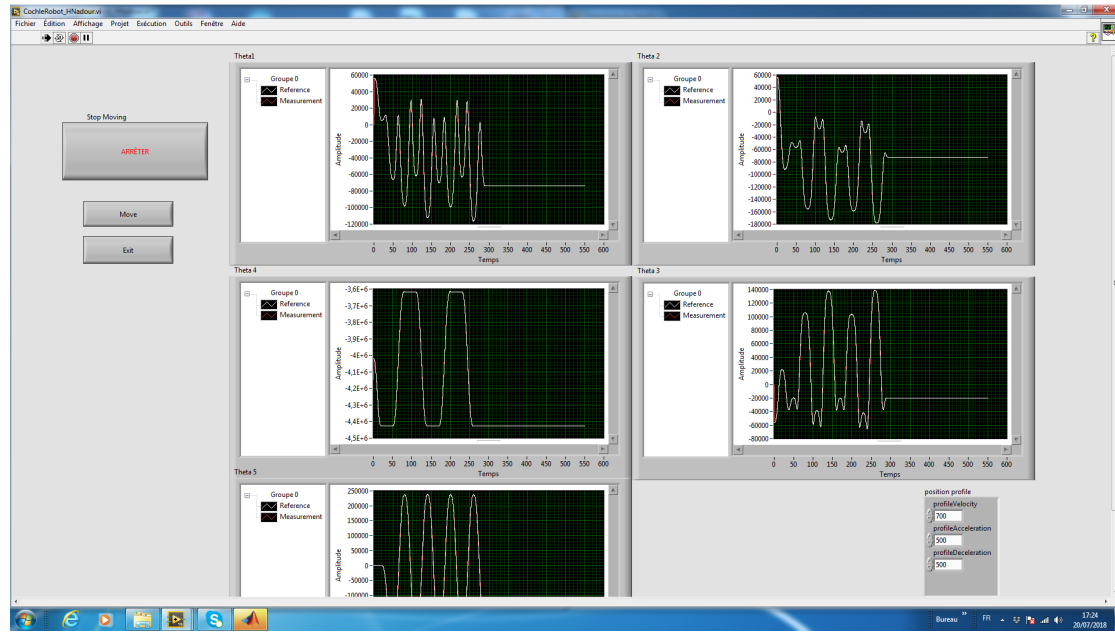


Figure 4.21: The motors angels and the references (screen capture for LabVIEW)

Chapter 5

Conclusion and perspectives

Contents

In the light of curing the hearing loss by treating the inner cochlea with therapeutic Paramagnetic Nanoparticles instead of any manual access that may damage it, through this work, we could realize a novel manipulator robot of 5 DoF in order to position a magnetic actuator around the patient head to guide those magnetic particles in the inner ear.

To do that, a fully list of specifications were to be put like the works space, the necessary and sufficient degrees of freedom, taking in account the compactness together with precision and rigidity as well.

According to the specifications desired for the task, and after analysing the preliminary works done before in the project together with some other relevant medical mechanisms, A novel mechanism, that can fulfil all the required specifications, was mandatory. The second chapter discussed this point showing the rational behind the choice of the mechanism, as well as the choice of its dimensions and motorisations; The trajectory of cochlea and the shape of the enclosed works space wanted to be reached, in addition to the compactness and safety of the patient, made the spherical RCMs the best mechanism to be chosen in order to generate rotational movements; among multiple spherical RCMs proposed in some articles and in this report, we have chosen the most convenient one; Furthermore, the necessity for linear movements pushed us to add another mechanism in addition to the first one, the delta structure was the best choice for multiple reasons, especially for its precision since the head organs (like the cochlea) to be travelled by the attractive point are so small, Beside to this feature, the rigidity of parallel structure is vital to bear the magnetic actuator. Combining the two structures yields an hybrid mechanism (serial and parallel), this robot was portrayed and designed by the

mean of SolidWorks.

In the chapter of Medeling, the different necessary models (Geometric, Kinematic, and Dynamic models) were established to demonstrate the system state model and control it as well. Additionally, *we demonstrated two novel models (inverse and direct geometric models) for the delta structure.*

The last chapter was dedicated for tuning a control law, explaining the rational point behind the strategy that allowed us to introduce easily controllers like PI and Loop-shaping.

As For simulation, we used Simmechanics, after exporting the structure designed using Solidworks, to validate the different models and the tuned control law. the results was satisfying for both the modeling and control.

Finally, After printing the different mechanism organs, they were jointed together to make a prototype controlled via a computer using LabVIEW software and Maxon controllers.

Two important points might be considered as perspectives :

In order to increase the volume of the space work to be travelled, and potentially the compactness, it is worthy to study the space work of the delta structure based on its lengths l_1 , l_2 , and L (the distance between L_2 and the nacelle center P). l_0 and l_3 are doomed to be invariable (or variable in very short range) by the constraints on the motors lengths and the end-effector.

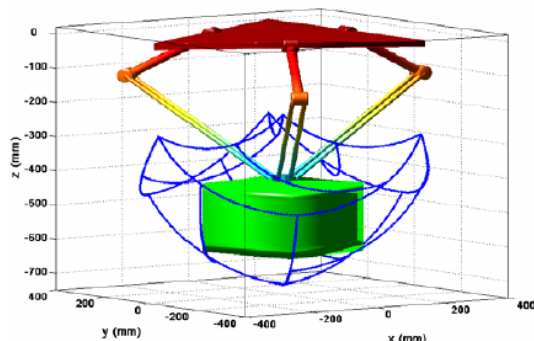


Figure 5.1: A cube inside the work space of the delta robot [5]

The rigorous tuning of the dimensions was supposed to be done this way, but for time reason we decided to use Geogebra instead.

Also, it is possible to introduce telescopic arm as demonstrated as it is pointed to in the following figure:



Figure 5.2: Delta robot of 4 degrees of freedom

Usually, this arm is used to generate another rotational degree of freedom for the end-effector. Notwithstanding, there is no need to another degree of freedom in our case, but it can be used to change the angle separating the permanent magnets of the actuator (figure2.1), as result the distance L between the attractive point L_2 and the nacelle center can be changed. this is very useful to have a flexible work of space for the delta structure. That way it is even possible to cover all the head space.

Bibliography

Contents

- [1] Emmanuel Deruty. How the ear works, 2011. Available at <https://www.soundonsound.com/sound-advice/how-ear-works>.
- [2] Manel Abbes, Mouna Souissi, Karim Belharet, Hassen Mekki, and Gerard Poisson. A novel remote-center-of-motion serial manipulator for inner ear drug delivery. In *International Conference on Advanced Intelligent Mechatronics*. IEEE, 2018.
- [3] Walid Amokrane, Karim Belharet, Mouna Souissi, Alexis Bozorg Grayeli, and Antoine Ferreira. Design and prototyping of a magnetic actuator based permanent magnets for microbead navigation in viscous environment. In *Intelligent Robots and Systems (IROS), 2017 IEEE/RSJ International Conference on*, pages 395–400. IEEE, 2017.
- [4] EP McCarthy. Phase lead compensator design. *Electronics Letters*, 26(21):1817–1819, 1990.
- [5] Toufik BENTALEB, Labo Mécanique des Structures, Med El Amine BELOUCHRANI, Labo Génie des Matériaux, and Noureddine HENINI. Analyse de l'exactitude dun robot parallèle delta. In *4th Conference Internationale sur la Productique, CIP, Setif, Algeria*, 2007.
- [6] Tabish Mustafa. *An image-guided robotic assistant for microsurgery of the inner ear*. PhD thesis, Master thesis, Johns Hopkins University, 2005.
- [7] Xinsheng Gao, Youdan Wang, Kejian Chen, Brian P Grady, Kenneth J Dormer, and Richard D Kopke. Magnetic assisted transport of plga nanoparticles through a human round window membrane model. *Journal of Nanotechnology in Engineering and Medicine*, 1(3):031010, 2010.

BIBLIOGRAPHY

- [8] SK Juhn. Barrier systems in the inner ear. *Acta Oto-Laryngologica*, 105(sup458):79–83, 1988.
- [9] OLIVIER Sterkers, EVELYNE Ferrary, and CLAUDE Amiel. Production of inner ear fluids. *Physiological reviews*, 68(4):1083–1128, 1988.
- [10] Chi-Sung Han, Jong-Ryul Park, Sung-Hyun Boo, Joon-Man Jo, Kyung-Won Park, Won-Yong Lee, Joong-Gi Ahn, Myung-Koo Kang, Byung-Gun Park, and Hyun Lee. Clinical efficacy of initial intratympanic steroid treatment on sudden sensorineural hearing loss with diabetes. *Otolaryngology—Head and Neck Surgery*, 141(5):572–578, 2009.
- [11] Khalid S Alzamil and Fred H Linthicum Jr. Extraneous round window membranes and plugs: possible effect on intratympanic therapy. *Annals of Otology, Rhinology & Laryngology*, 109(1):30–32, 2000.
- [12] Alec N Salt. Dexamethasone concentration gradients along scala tympani after application to the round window membrane. *Otology & neurotology: official publication of the American Otological Society, American Neurotology Society [and] European Academy of Otology and Neurotology*, 29(3):401, 2008.
- [13] Erin E Leary Swan, Mark J Mescher, William F Sewell, Sarah L Tao, and Jeffrey T Borenstein. Inner ear drug delivery for auditory applications. *Advanced drug delivery reviews*, 60(15):1583–1599, 2008.
- [14] Alec N Salt and Yilong Ma. Quantification of solute entry into cochlear perilymph through the round window membrane. *Hearing research*, 154(1-2):88–97, 2001.
- [15] Yann Nguyen, Mathieu Miroir, Guillaume Kazmitcheff, Evelyne Ferrary, Olivier Sterkers, and Alexis Bozorg Grayeli. Super paramagnetic nanoparticles delivery through a microcatheter by solenoids. In *Nano/Molecular Medicine and Engineering (NANOMED), 2010 IEEE 4th International Conference on*, pages 153–157. IEEE, 2010.
- [16] Elizabeth G Quate, Kevin G Wika, Michael A Lawson, George T Gillies, RC Ritter, MS Grady, and MA Howard. Goniometric motion controller for the superconducting coil in a magnetic stereotaxis system. *IEEE Transactions on Biomedical Engineering*, 38(9):899–905, 1991.
- [17] Shigehiro Nishijima and Shin-ichi Takeda. Superconducting high gradient magnetic separation for purification of wastewater from paper factory. *IEEE transactions on applied superconductivity*, 16(2):1142–1145, 2006.

BIBLIOGRAPHY

- [18] J-B Mathieu, Gilles Beaudoin, and Sylvain Martel. Method of propulsion of a ferromagnetic core in the cardiovascular system through magnetic gradients generated by an mri system. *IEEE Transactions on Biomedical Engineering*, 53(2):292–299, 2006.
- [19] Karim Belharet, David Folio, and Antoine Ferreira. Endovascular navigation of a ferromagnetic microrobot using mri-based predictive control. In *Intelligent Robots and Systems (IROS), 2010 IEEE/RSJ International Conference on*, pages 2804–2809. IEEE, 2010.
- [20] MO Schurr, G Buess, B Neisius, and U Voges. Robotics and telemanipulation technologies for endoscopic surgery. *Surgical endoscopy*, 14(4):375–381, 2000.
- [21] Shuxiang Guo, Toshio Fukuda, and Kinji Asaka. A new type of fish-like underwater microrobot. *Ieee/Asme Transactions on Mechatronics*, 8(1):136–141, 2003.
- [22] Jon Edd, Sébastien Payen, Boris Rubinsky, Marshall L Stoller, and Metin Sitti. Biomimetic propulsion for a swimming surgical micro-robot. In *Intelligent Robots and Systems, 2003.(IROS 2003). Proceedings. 2003 IEEE/RSJ International Conference on*, volume 3, pages 2583–2588. IEEE, 2003.
- [23] Bahareh Behkam and Metin Sitti. Design methodology for biomimetic propulsion of miniature swimming robots. *Journal of Dynamic Systems, Measurement, and Control*, 128(1):36–43, 2006.
- [24] Sylvain Martel, Jean-Baptiste Mathieu, Ouajdi Felfoul, Arnaud Chanu, Eric Aboussouan, Samer Tamaz, Pierre Pouponneau, LHocine Yahia, Gilles Beaudoin, Gilles Soulez, et al. Automatic navigation of an untethered device in the artery of a living animal using a conventional clinical magnetic resonance imaging system. *Applied physics letters*, 90(11):114105, 2007.
- [25] Michael P Kummer, Jake J Abbott, Bradley E Kratochvil, Ruedi Borer, Ali Sengul, and Bradley J Nelson. Octomag: An electromagnetic system for 5-dof wireless micromanipulation. *IEEE Transactions on Robotics*, 26(6):1006–1017, 2010.
- [26] Serhat Aksungur. Remote center of motion (rcm) mechanisms for surgical operations. *International Journal of Applied Mathematics, Electronics and Computers*, 3(2):119–126, 2015.
- [27] Amir Molaei, Ebrahim Abedloo, Hamid D Taghirad, and Zahra Marvi. Kinematic and workspace analysis of diamond: An innovative eye surgery robot.

BIBLIOGRAPHY

- In *Electrical Engineering (ICEE), 2015 23rd Iranian Conference on*, pages 882–887. IEEE, 2015.
- [28] Lama Al Bassit. *Structures mécaniques à modules sphériques optimisées pour un robot médical de télé-échographie mobile*. PhD thesis, Université d'Orléans, 2005.
 - [29] Meryam Rachedi, Mohamed Bouri, and Boualem Hemici. Application of an h control strategy to the parallel delta. In *Communications, Computing and Control Applications (CCCA), 2012 2nd International Conference on*, pages 1–6. IEEE, 2012.
 - [30] Reymond Clavel. *Conception d'un robot parallèle rapide à 4 degrés de liberté*. EPFL, 1991.
 - [31] Alain Codourey. Dynamic modelling and mass matrix evaluation of the delta parallel robot for axes decoupling control. In *Intelligent Robots and Systems' 96, IROS 96, Proceedings of the 1996 IEEE/RSJ International Conference on*, volume 3, pages 1211–1218. IEEE, 1996.
 - [32] Wisama Khalil and Etienne Dombre. *Modeling, identification and control of robots*. Butterworth-Heinemann, 2004.
 - [33] Alain Codourey. *Contribution à la commande des robots rapides et précis*. EPFL, 1991.